

<b>REPORT DOCUMENTATION PAGE</b>			<b>Form Approved OMB No. 0704-0188</b>	
Public reporting burden for this collection of information is estimated to average 1 hour per response, including the time for reviewing instructions, searching data sources, gathering and maintaining the data needed, and completing and reviewing the collection of information. Send comments regarding this burden estimate or any other aspect of this collection of information, including suggestions for reducing this burden to Washington Headquarters Service, Directorate for Information Operations and Reports, 1215 Jefferson Davis Highway, Suite 1204, Arlington, VA 22202-4302, and to the Office of Management and Budget, Paperwork Reduction Project (0704-0188) Washington, DC 20503.				
<b>PLEASE DO NOT RETURN YOUR FORM TO THE ABOVE ADDRESS.</b>				
<b>1. REPORT DATE (DD-MM-YYYY)</b> 14-07-2010		<b>2. REPORT TYPE</b> Final Technical		<b>3. DATES COVERED (From - To)</b> 13-11-2007 - 11-11-2009
<b>4. TITLE AND SUBTITLE</b> STTR (PHASE II) - STABILITY MODELS FOR AUGMENTOR DESIGN TOOLS AND TECHNOLOGY ASSESSMENT			<b>5a. CONTRACT NUMBER</b> FA9550-08-C-0039	
			<b>5b. GRANT NUMBER</b> 	
			<b>5c. PROGRAM ELEMENT NUMBER</b> 65502F	
<b>6. AUTHOR(S)</b> Shoreh Hajiloo / Hung Le Cascade Tehnologies, Inc.			<b>5d. PROJECT NUMBER</b> STTR	
			<b>5e. TASK NUMBER</b> TX	
			<b>5f. WORK UNIT NUMBER</b> 	
<b>7. PERFORMING ORGANIZATION NAME(S) AND ADDRESS(ES)</b> Cascade Technologies, Inc. 2445 Faber Place, Suite 100 Palo Alto, CA 94303			<b>8. PERFORMING ORGANIZATION REPORT NUMBER</b> 	
<b>9. SPONSORING/MONITORING AGENCY NAME(S) AND ADDRESS(ES)</b> Air Force Office of Scientific Research 875 N. Randolph Street Arlington, VA 22203-1768			<b>10. SPONSOR/MONITOR'S ACRONYM(S)</b> AFOSR	
			<b>11. SPONSORING/MONITORING AGENCY REPORT NUMBER</b> AFRL-OSR-VA-TR-2012-0049	
<b>12. DISTRIBUTION AVAILABILITY STATEMENT</b> Unclassified. Reproduction in whole or in part is permitted for any purpose of the United States Government; its distribution is unlimited.				
<b>13. SUPPLEMENTARY NOTES</b>				
<b>14. ABSTRACT</b> The objective of the project was to design and study new flame stabilizers for augmentor systems that could lead to improved static flame stability. The project consisted of (a) development of new augmentor flame holder designs and their experimental characterization; and (b) demonstration of numerical predictions of the flame behavior using the resulting experimental designs and measurements. Four flame configurations were considered in the both experiments and computations: partially premixed flame in high temperature vitiated flow and in room temperature air flow, fully premixed flame and hybrid of fully-partially premixed flame. All studies demonstrated improved static flame stability of the new flame holder. Computations results, which used Damköhler number similarity, compared well generally with those from experiments. However, simulations showed that flames remain attached to the bluff body, and formed on the edge of the body wake; but these features were not observed in experiments.				
<b>15. SUBJECT TERMS</b> Computational, geometries, prototype, premixed, flame and hybrid, augmentor, turbulent combustion				
<b>16. SECURITY CLASSIFICATION OF:</b>			<b>17. LIMITATION OF ABSTRACT</b> None	<b>18. NUMBER OF PAGES</b> 68
<b>a. REPORT</b> Unclassified	<b>b. ABSTRACT</b> Unclassified	<b>c. THIS PAGE</b> Unclassified	<b>19a. NAME OF RESPONSIBLE PERSON</b> Dr. Julian Tishkoff	
			<b>19b. TELEPHONE NUMBER (Include area code)</b> 703-696-8478	

**AF06-T033**

**Stability Models for Augmentor Design Tools and  
Technology Assessment**

Contractor:  
Cascade Technologies, Inc.  
2445 Faber Pl., Ste 100  
Palo Alto, CA 94303

Contract number:  
FA9550-08-C-0039

*Principal Investigators:*  
Dr. Shoreh Hajiloo / Dr. Hung Le  
Cascade Technologies, Inc.

Prof. Godfrey Mungal  
Stanford University.

Reporting period:  
11/13/07 - 11/11/09

# Contents

<b>1</b>	<b>Introduction and Project Objectives</b>	<b>5</b>
<b>2</b>	<b>Flame Holder Development</b>	<b>5</b>
2.1	Experimental Setup and Flame Holder Design . . . . .	5
2.1.1	Setup . . . . .	5
2.1.2	Implementation of Premixed Burner . . . . .	7
2.1.3	Basic Bluff-Body Design . . . . .	7
2.1.4	Implementation of the Cooling Capability . . . . .	8
2.1.5	Implementation of the Turbulence Grid . . . . .	8
2.1.6	Implementation of Stereo PIV . . . . .	8
2.1.7	CH Chemiluminescence Detection . . . . .	9
2.2	Lift-Off Experiment . . . . .	9
2.2.1	Preliminary Geometric Modifications of the Bluff Body Base . . . . .	9
2.2.2	Measurement of Flame Liftoff Heights . . . . .	11
2.2.3	Design Optimization (D+S, T+S Cavities) . . . . .	12
2.2.4	Dependence of the Liftoff Heights on Cavity Depths and Placements . . .	13
2.2.5	Summarizing Plot of Liftoff Height Measurements . . . . .	13
2.2.6	Velocity Fields Obtained from Stereo PIV . . . . .	15
2.2.7	Vorticity and Strain Rate Fields . . . . .	23
2.2.8	Summarizing Schematics of Flow Patterns with Local Cavity Geometries	27
2.3	Blowout Study . . . . .	29
2.3.1	Variation of Flame Configuration . . . . .	29
2.3.2	Gas Chromatography for Measuring Methane Concentration . . . . .	29
2.3.3	Blowout Limit Measurements . . . . .	29
2.3.4	Measurements of Methane Mole Fraction Field . . . . .	31
2.3.5	Flow Fields Near the Base in a Room Temperature Freestream (2D PIV Measurement) . . . . .	36
2.3.6	Swirling Strengths and Strain Rates Near the Base in a Room Temperature Freestream . . . . .	38
<b>3</b>	<b>Numerical Modeling Using Large-Eddy Simulation</b>	<b>40</b>
3.1	Damköhler Number Similarity for Static Flame Stability in Augmentor Flows . .	40
3.1.1	Introduction . . . . .	40
3.1.2	Numerical Formulation . . . . .	42
	Filtered Flow Equations . . . . .	42
	Flamelet Progress Variable Approach . . . . .	43
	Non-Dimensional Governing Equations . . . . .	45
	Damköhler Number Similarity . . . . .	47

3.1.3	Numerical Method . . . . .	50
3.1.4	Results . . . . .	51
3.1.5	Conclusion . . . . .	55
3.2	Large-Eddy Simulations of New Flame Holder Geometries . . . . .	55
3.2.1	Test Cases and Simulation Setup . . . . .	58
3.2.2	Sub-Filter Models and Numerical Schemes . . . . .	59
3.2.3	Results . . . . .	59
3.2.4	Effect of Crossflow Temperature . . . . .	62
3.2.5	Effect of Lewis number Approximation . . . . .	62
3.2.6	Conclusions . . . . .	62
<b>Appendix A</b>		<b>64</b>
A.1	Contributors . . . . .	64
A.2	Related Publications & Presentations . . . . .	64

## Abstract

The overall objective of the project was to design and study new flame stabilizers for augmentor systems that lead to improved static flame stability. For this purpose, the project consisted of two major activities: (a) development of new augmentor flame holder designs with improved static flame stability, and their experimental characterization; and (b) demonstration of numerical predictions of the flame behavior using the resulting experimental designs and measurements.

The experimental studies investigated the effect of cavity-based geometries under the following four flame configurations: (i) partially premixed flame in high temperature vitiated flow; (ii) partially premixed flame at room temperature air flow; (iii) fully premixed flame; and (iv) hybrid fully and partially premixed flames. The first flame condition was used to study the effect on liftoff heights. Blowout studies were conducted in the remaining three flame conditions. All studies demonstrated improved static flame stability of the new flame holders. This behavior was explained using measurements of species, temperature, and velocity field.

Based on the selected flame-holder configurations from experiments, two computational modeling studies were conducted to establish a new formulation of Damköhler number similarity and to assess new combustion modeling techniques to predict static stability of the flame-holder.

Simulations of flow and combustion for the new flame holder designs compared qualitatively well with the experiments. However, there were disagreements between simulation and experimental results. In the simulations, the flames remained attached to the bluff body for all cases and flames formed on the edge of the bluff body wake. Both these features were not seen in the experiments. It was speculated that the reason for disagreement was a higher level of inflow turbulence in the experiment or a very non-isotropic flow induced by the turbulence mesh. However further investigation is required.

# 1 Introduction and Project Objectives

The overall objective of the project was to design and study new flame stabilizers for augmentor systems that lead to an improved static flame stability computationally and experimentally. The main objectives of the project were: i) development of various newly designed bluff body (augmentor) bases, ii) experimental investigation of static flame stability with the various prototype base geometries, and iii) demonstration of numerical predictions of the experiments. In accordance with these objectives, the experimental studies focused on proposing local cavity-based base geometries and investigating their effect on liftoff heights and blowout limits for the following flame configurations: i) a partially premixed flame in a high temperature vitiated flow (liftoff study); ii) a partially premixed flame in room temperature air flow (blowout study); iii) a fully premixed flame (blowout study); and iv) hybrid fully and partially premixed flames (blowout study). The detailed experimental results of the liftoff and blowout studies will be discussed in section 2. The computational studies will be presented in section 3. Two different computational approaches were used to assist in the development of new flame-holding technologies. The first was a new formulation of Damköhler (Da) number similarity. This technique allowed for a proper definition of Da, such that similarity conditions was defined for the assessment of flame stabilization. With this method, the assessment of afterburner static stability under typical operating conditions could be performed using low-speed experiments. The second was an assessment of the combustion modeling techniques to predict static stability of the flame-holder configurations presented in Section 2.

## 2 Flame Holder Development

### 2.1 Experimental Setup and Flame Holder Design

#### 2.1.1 Setup

As shown in Fig. 1, the experimental setup for the liftoff study consisted of six parts: i) a main premixed burner to provide post-combustion gases in the vicinity of a bluff body, ii) a bluff body through which methane fuel was injected to form jets in crossflow with the high-temperature post-combustion stream, iii) an additional cooling capability in the post-combustion stream of the premixed burner and upstream of the bluff body to control the vitiated air temperature, iv) a turbulence grid to mimic high-Reynolds number effects, v) a stereo PIV system to measure the local free-stream speed and the velocity fields in the vicinity of the bluff body, and vi) an intensified camera for CH chemiluminescence detection by which the liftoff heights of the methane diffusion flame were characterized. In the following sections, a detailed description of the experimental facility is provided.

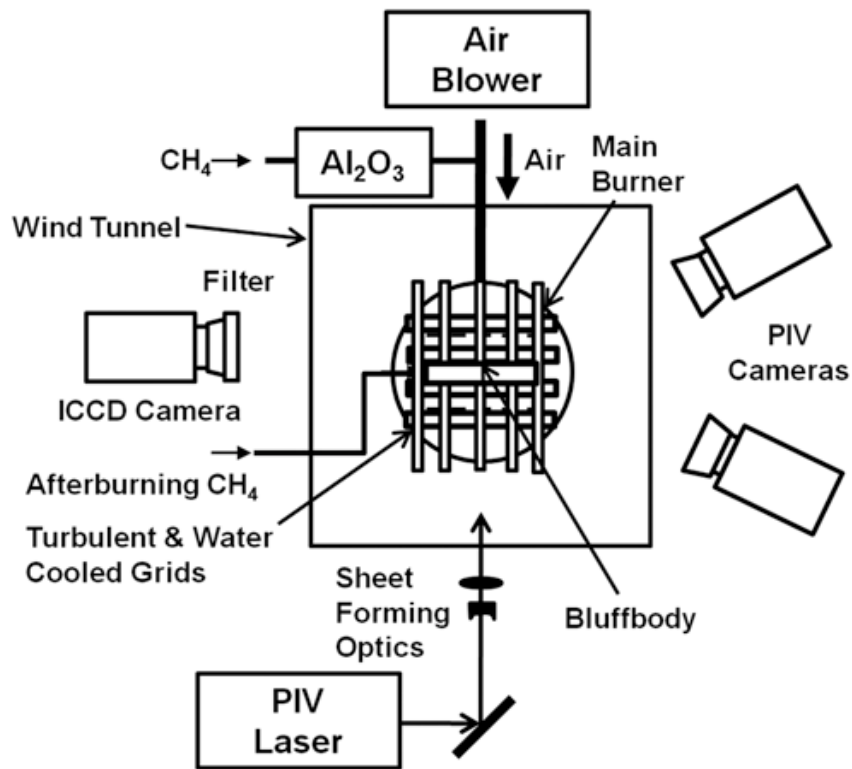


Figure 1: Schematic of the top view of the experimental setup

### 2.1.2 Implementation of Premixed Burner

The premixed burner (on loan from Professor Robert Dibble's lab at University of California, Berkeley) was located centrally in a 50 cm  $\times$  50 cm cross-sectional area vertical wind tunnel. The wind tunnel could generate 3.5 m/s flow. The burner had 2184 holes, each having a diameter of 1/16 inch on the top surface. The top surface had an overall diameter of 8.27 inches to allow the array of tiny flames to generate a uniform temperature profile over a wide region. Air was delivered by a 1.5 hp blower and was mixed with methane approximately 3 m upstream of the burner exit. The equivalence ratio of the methane/air mixture was kept fixed at 0.64 in the current study. Furthermore, the resulting temperature and speed of the post combustion gas were  $\approx 1315$  K and 5.7 m/s.

### 2.1.3 Basic Bluff-Body Design

The key issues in the bluff body flame holder design were the geometrical shape of the flame holder, the dimensions, and the ability of the material to survive in the high temperature environment. The basic geometry was chosen in consultation with Dr. Jeffrey Lovett from Pratt & Whitney and Dr. Marios Soteriou from United Technologies Research Center. As shown in Fig. 2, the basic geometry of the bluff body consisted of a 4.5 inches long, 1 inch thick, and 6 inches wide rectangular body with a 1/2 inch radius rounded nose. A porous ceramic (fused silica, 63 % nominal porosity), which is machinable, has high service temperature ( $\approx 2000$  K), and has good resistance to thermal crack propagation, was used to build the bluff body. The high service temperature eliminated the need for complex cooling. Methane was delivered from

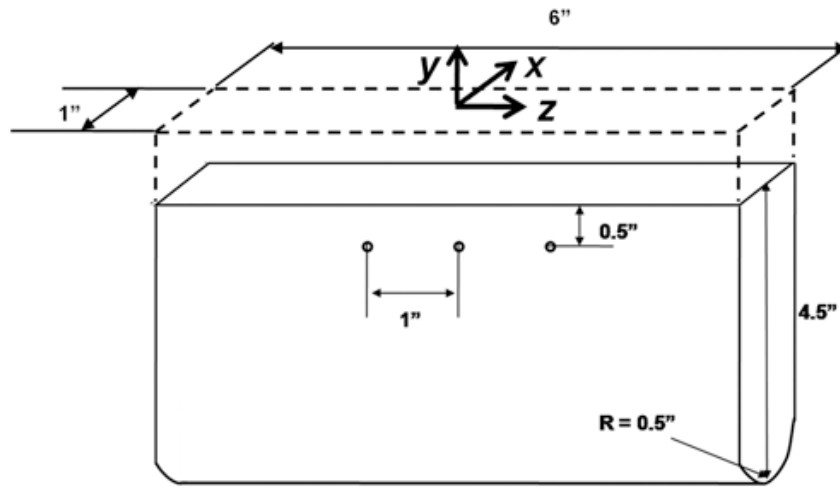


Figure 2: Detailed schematic of the bluff body.

six 1/8 inch (OD) fuel injection nozzles (three on each side) branched from a single 3/8 inch OD fuel delivery pipe. The nozzles, which were located 1/2 inch upstream of the base of the bluff



body with 1-inch spacing, produced two sets of opposing jets in the crossflow. Throughout the study, the initial speed of the methane jet and the corresponding square root of the momentum ratio ( $r$ ) between the individual methane jets and the crossflow were kept fixed at  $\approx 3.7$  m/s and  $\approx 0.9$ , respectively. The origin of the coordinate system was placed on the symmetry planes of the bluff body and 1 inch downstream of the physical base, as shown in Fig. 2. Furthermore, the dotted volume in Fig. 2 would be filled later with various physical inserts.

#### 2.1.4 Implementation of the Cooling Capability

The copper water-cooled grid, which has a geometry similar to the condenser coil of a refrigerator, was placed on the top of the main burner to control the temperature of the vitiated flow. Water at room temperature flowed through a 1/4 inch (OD) serpentine-shaped copper tube that had 11 turns within a 15 inches by 18 inches rectangular region. Numerous 1/16 inch (OD) copper wires were welded on the copper tube to improve the heat conduction along the streamwise direction of the water flow. Using the water cooled grid, we were able to reduce the temperature of the post-combustion gas by  $\approx 100$  K from its original temperature, which was at  $\approx 1400$  K. The ability to reduce the temperature was an important aspect of this study, because without this reduction, the methane jets ignited immediately upon exiting, whereas with the cooler free-stream, the jets mixed with the free-stream and only ignited in the wake of the bluff body.

#### 2.1.5 Implementation of the Turbulence Grid

The turbulence grid was placed  $\approx 1$  inch downstream of the top surface of the water-cooled grid. The water-cooled grid was composed of two, top and bottom, layers of 1/2 inch OD, 8 inch long ceramic (99.9%  $\text{Al}_2\text{O}_3$ ) tube arrays. Each array was formed by 6 parallel-placed ceramic tubes with 1.25 inches inter-distance (36 % open area). The top and bottom arrays were placed perpendicular to each other such that the open area became an exact square. Using the grid, we could increase the freestream turbulent fluctuation from  $\approx 5$  % (with no grid) to 8 % (with the grid).

#### 2.1.6 Implementation of Stereo PIV

For the PIV studies, 3  $\mu\text{m}$  nominal diameter  $\text{Al}_2\text{O}_3$  particles were seeded into the flow, and a  $\approx 100$  mJ/pulse (532 nm) double-pulsed Nd:YAG laser (New Wave, Gemini PIV) with  $\approx 1$  mm sheet-thickness was used to illuminate the particles. The  $\text{Al}_2\text{O}_3$  particles were mixed densely with the methane and air streams such that adequate seeding density could be achieved even in the high temperature environment. The resulting Mie scattering was detected by two double-exposure CCD cameras (La Vision, Flow Master) mounted with a  $70^\circ$  included angle.

### 2.1.7 CH Chemiluminescence Detection

The mean and fluctuating components of the flame liftoff height were used as a criterion for the performance of various bluff body geometries tested in the current study. Intensified and filtered imaging of CH chemiluminescence was carried out to measure the liftoff height. For this imaging, an intensified camera (Princeton Instrument, PI-MAX) with a gate width of  $100 \mu\text{s}$  and a  $\approx 4305$  nm band pass filter was used. Representative examples of the instantaneous chemiluminescence images are provided in Fig. 3. The white dotted lines represent the instantaneous location of the flame base. From each image, the flamebase location was determined manually and the obtained locations from 200 images were ensemble averaged.

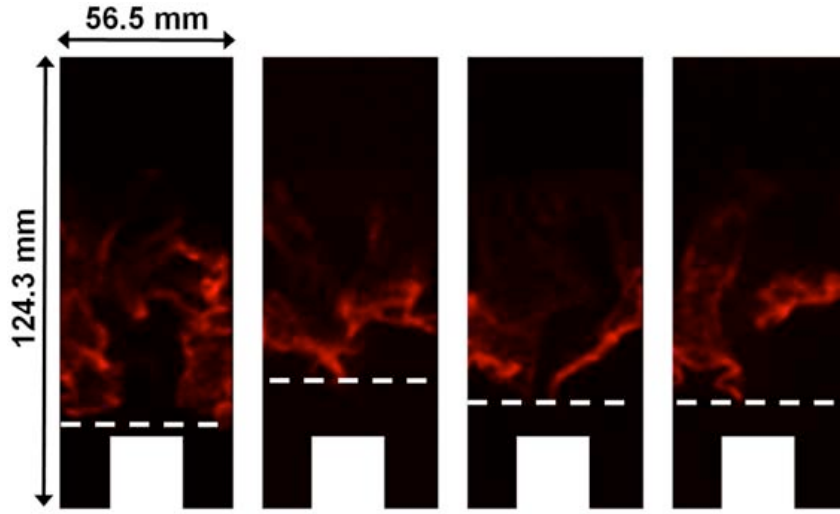


Figure 3: Representative instantaneous images of intensified chemiluminescence. Gate width was 100 ms. White dotted lines represent the instant locations of the flamebase.

## 2.2 Lift-Off Experiment

### 2.2.1 Preliminary Geometric Modifications of the Bluff Body Base

The base geometry of the bluff body was modified by addition of blocks with different shapes to the dotted region in Fig. 2. Nine 7 inch long blocks with different cross-sections, as shown in Fig. 4, were used. The blocks were categorized with respect to their shape as Reference (R), V cavity, D cavity, S or R+S cavity, and T and I blocks. The Reference case (R) was a solid block extension with one inch square cross section. The R block modified the geometry by increasing the height of the bluff body to 5.5 inches. The fuel injection holes were unchanged, and, therefore, the Reference case modified the setup by moving the fuel injection jets in the upstream direction by 1 inch. The Reference case was used to form the V cavity block by cutting a 0.43 inch deep V shape with angle  $60^\circ$  along the block (see Fig. 4b for its detailed

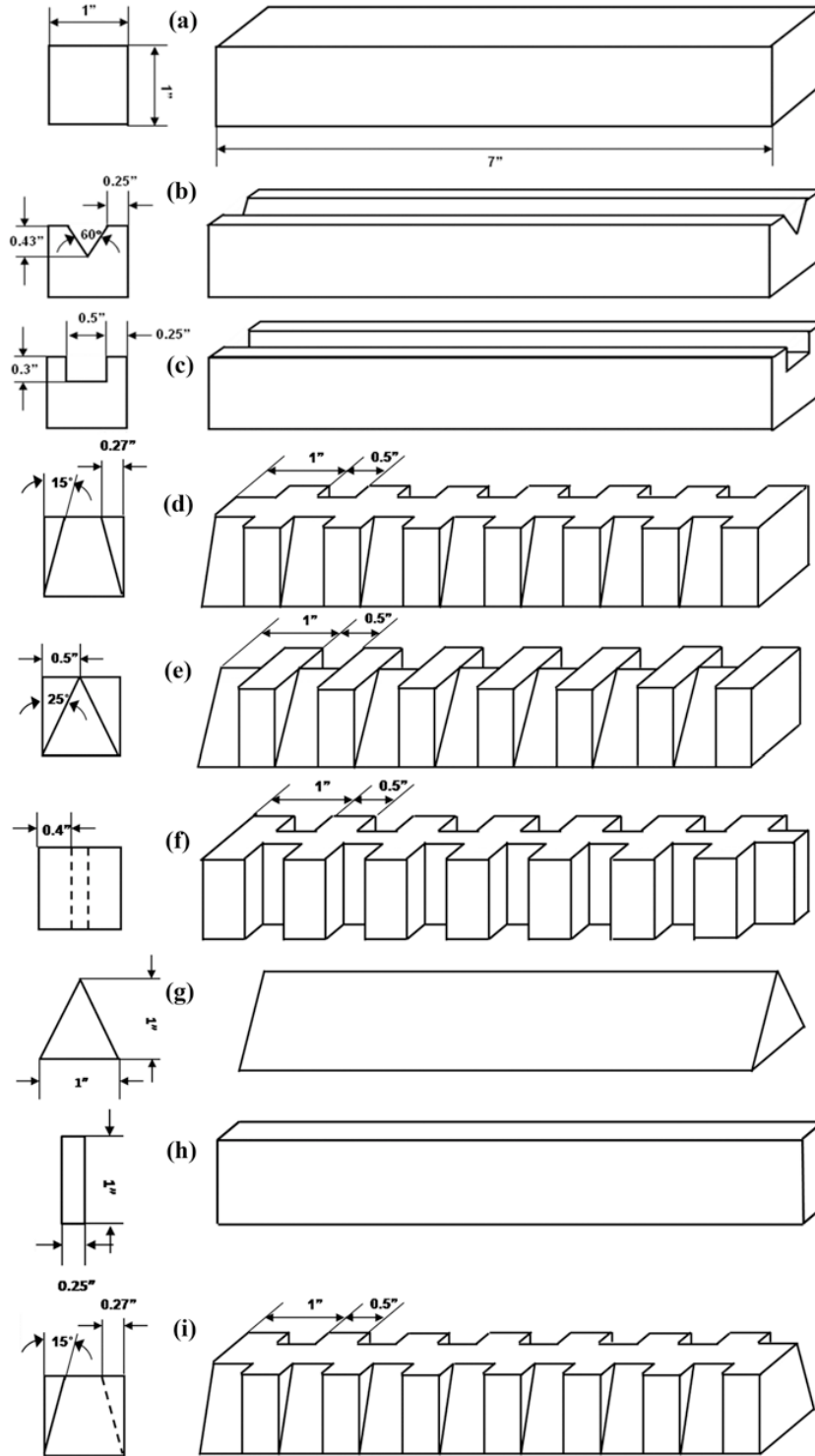


Figure 4: Schematics of various blocks. (a) Reference (or R), (b) V cavity, (c) D cavity, (d) 15° S cavity, (e) 25° S cavity, (f) 90° S cavity (or R+S), (g) T, (h) I, and (i) 15° S cavity-out-of-phase geometries.

dimensions). Similarly, the D cavity block was constructed by cutting a 0.3 inch deep, 0.5 inch wide rectangular shape, as shown in Fig. 4c. The S cavities had a more complex shape, formed from the Reference case by cutting 0.5 inch wide individual side-wise cavities with  $15^\circ$  (Figs. 4d and 4i),  $25^\circ$  (Fig. 4e), and  $90^\circ$  (Fig. 4f) slopes, respectively. (The inclined design was motivated by the fastback designs used in automobile designs, where the flow pattern changed based upon inclination angle. For details see Sovran *et al.* (1978)). The cavities were 1 inch apart and were in phase with the three fuel nozzles for cases d, e, and f, whereas case i was designed to be out of phase. The effect of in-phase and out-of-phase geometries will be discussed later. Furthermore, the T block (Fig. 4g) had an equilateral triangular shape with 1-inch height and 1-inch base length. Addition of the T block resulted in two symmetric recirculation zones. Finally, as shown in Fig. 4h, the I geometry had a  $0.25 \text{ inch} \times 1 \text{ inch}$  rectangular cross section.

### 2.2.2 Measurement of Flame Liftoff Heights

Figure 5 shows the ensemble-averaged flame liftoff height for each different case discussed in section 2.2.1. For all cases the temperature of the post-combustion gas, the cross flow speed,

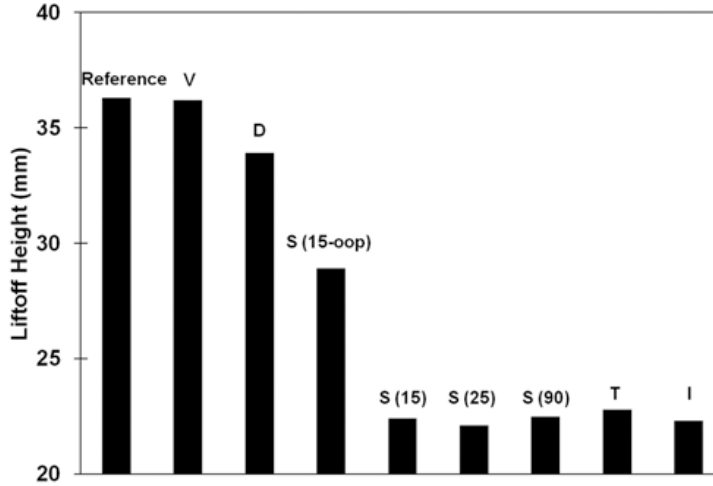


Figure 5: Liftoff heights for various bluff body base designs. For all cases, the temperature and the speed of the crossflow and the square root of the momentum ratio between the high-temperature post-combustion gas and the injected methane are kept identical as 1300 K, 5.7 m/s, and  $\approx 0.9$ , respectively.

and the square root of the momentum ratio between high-temperature post-combustion gas and injected methane were kept identical at 1300 K,  $\approx 5 \text{ m/s}$ , and  $\approx 1$ , respectively. The equivalence ratio of the main burner was 0.63. The liftoff heights were determined by averaging individual liftoff heights from 200 randomly sampled CH chemiluminescence images of the flame. The liftoff height of the V cavity (36.2 mm) showed very marginal improvement in comparison with that of the Reference case ( $\approx 36.3 \text{ mm}$ ), while the D cavity (33.9 mm) showed a more noticeable

decrease of the liftoff height. The most significant improvement, however, was seen in the cases of the three S cavities (22.4 mm, 22.1 mm, and 22.5 mm for 15°, 25°, and 90° wall slopes, respectively) and the T (22.8 mm) and I (22.3 mm) geometries. The flame liftoff heights were not a strong function of the slope of the S cavities in the range investigated here even though their recirculation patterns and vortex structures could be noticeably different from each other (Sovran *et al.*, 1978).

### 2.2.3 Design Optimization (D+S, T+S Cavities)

Based on the results from the geometries discussed in Section 2.2.1, we refined our designs to benefit from the presence of both the D cavity (re-entrant shape) and the 90° S cavity, which introduced local three-dimensionality to form a so called D+S cavity block shown in Fig. 6a. The D cavity part was  $\approx 0.5$  inch deep and  $\approx 0.5$  inch wide, and the 90° S cavity is 0.5 inch wide, 1 inch high, and 0.4 inch deep. The T and the 90° S cavity were combined to build a so called T+S block shown in Fig. 6b. The S cavity was 0.5 inch wide and 0.25 inch deep (Shallow Cut T+S). The flame liftoff height measured in the identical flow condition as in Section 2.2.2 and

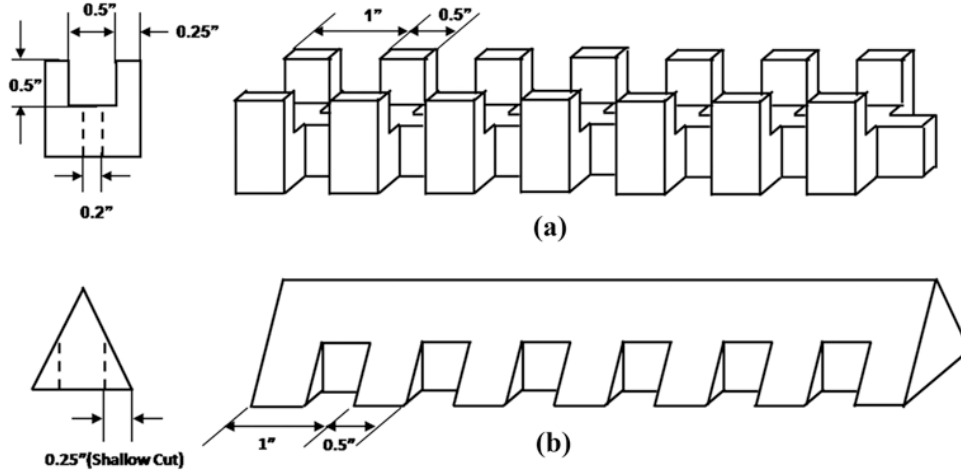


Figure 6: Schematics of (a) D+S cavity and (b) T+S geometries.

the cavity placement (in phase with the methane nozzle) with that of Fig. 5 was 17.4 mm in both cases, a 52 % liftoff height decreased in comparison with the Reference case. The flamebase in these cases mostly resided in the vicinity of (sometimes inside of) the S cavities, which resulted in less fluctuation of the flamebase (the standard deviations of the flamebase were  $\approx 7.5$  mm for D+S block and 7 mm for T+S block, respectively) when compared to that of the Reference case ( $\approx 13$  mm). We believed that local back steps (see Fig. 6) formed by the intersection of the D and S cavities and the T and S cavities might provide a desirable velocity field to maximize the flame stability, as well as the presence of the S cavity, which confined the injected methane to a more localized cavity region and prevents the methane jets from becoming excessively diluted

by the surrounding post-combustion gas. Such a locally fuel-rich (compared to its surrounding) cavity might act like a piloting region that assists in better holding of the overall downstream flame. It was, therefore, likely that this cavity fuel concentration effect would not be directly transferable to a flame configuration such as a fully premixed flame with a streamlined bluff body under far-upstream fuel injection that had been studied more recently in the literature (Shanbhogue *et al.*, 2009b). A more detailed description of the fuel concentration field will be discussed in the blowout study portion of the current report.

#### 2.2.4 Dependence of the Liftoff Heights on Cavity Depths and Placements

Figure 7a shows the liftoff height variation of the D+S cavity block using three different D cavity depths (0 inch, 0.5 inch, and 0.8 inch), whereas Fig. 7b shows the effect of different cavity placements with respect to the methane nozzle location, i.e., in-phase or out-of-phase cavities. Furthermore, Fig. 7 demonstrates the liftoff height dependence on the S cavity depth for the T+S geometry. In all three cases, the flow condition was identical to that of Section 2.2.2. From Fig. 7a the liftoff height for a moderate D cavity depth (17.4 mm) was significantly lower than that of the other two cases (22.5 mm in the 0 inch case and 33.2 mm in the 0.8 inch case). Neither the significantly shallow (0 inch case) nor the significantly deep D cavity depth (0.8 inch case) were optimal for flame stability. Hence, a D cavity with unity aspect ratio was better.

The effect of phase matching between the S cavity and the methane injection nozzle also played a central role in liftoff height, as shown in Fig. 7b. The liftoff height increased by more than 90 % by shifting the D+S cavity by a half period such that methane fuel was injected into a no-cavity region. The importance of the phase matching was also clear when different geometries were used. For example, the liftoff height of the completely in-phase 15° S cavity (Fig. 4d) was  $\approx 22.5\%$  lower than that of the half-in-phase/half-out-of-phase 15° S cavity (Fig. 4i). Additionally, the flame liftoff height was a function of the depth of the S cavity, as shown in Fig 7c. The liftoff height from a moderate S cavity depth (0.25 inch) showed a lower value than that of the 0 and 0.375-inch depth cases.

#### 2.2.5 Summarizing Plot of Liftoff Height Measurements

As shown in the summarizing plot (Fig. 8), the geometries containing local cavities (S cavities) with moderate aspect ratio and depth, especially the D+S and the T+S cavities placed in-phase with methane injection, showed over a 50 % decrease in the liftoff heights in comparison with the Reference case. In summary, the results shown here suggested that: (a) a combination of two- and three-dimensional changes to the base region (D+S and T+S) provided the lowest liftoff height; and (b) the alignment of the local cavities with the jet in crossflow resulted in optimal performance.

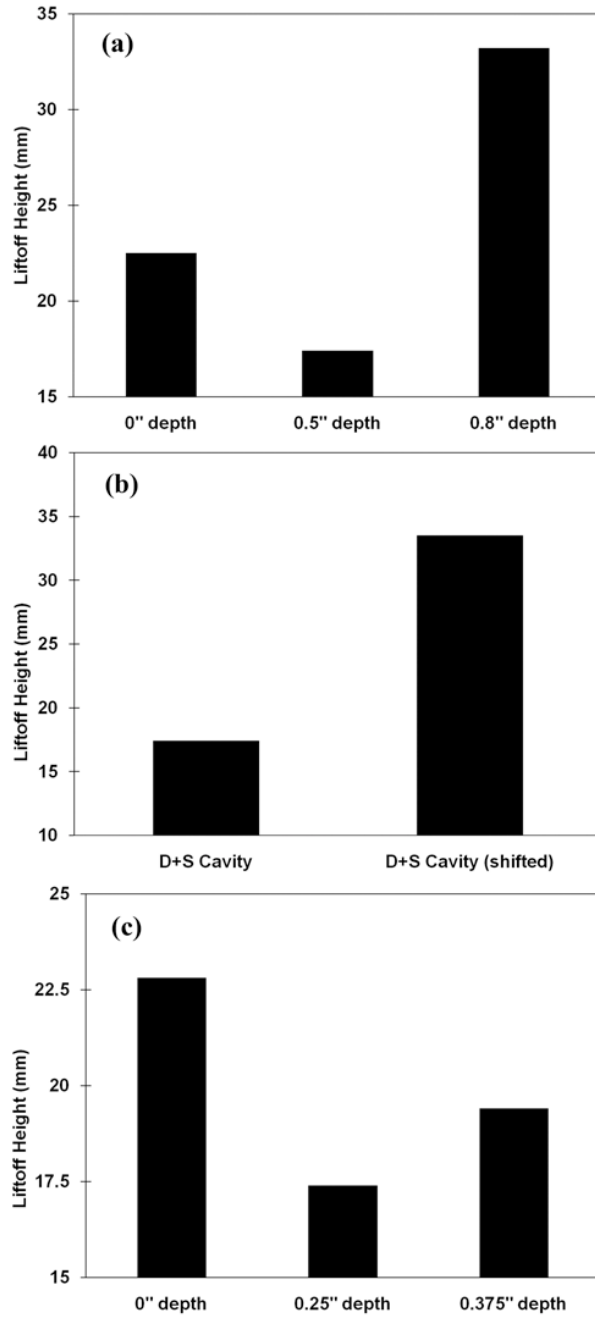


Figure 7: Liftoff height dependence on (a) the cavity depth (D cavity depth of the D+S cavity), (b) the placement of the bluff body base (D+S case), and (c) the S cavity depth (T+S case).

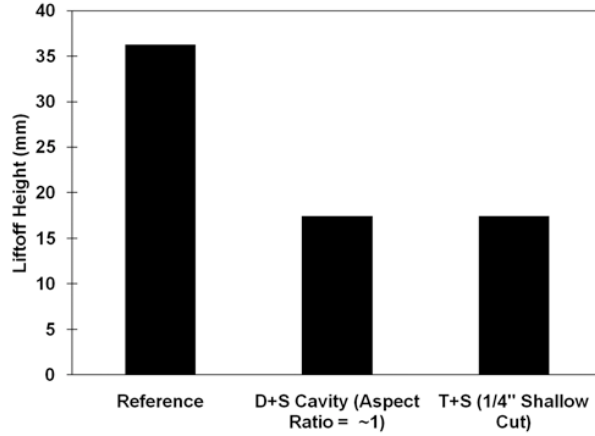


Figure 8: Minimum liftoff heights observed in the current study. The D+S geometry with moderate ( $\approx 1$ ) aspect ratio and the T+S geometry with 0.25 inch S cavity depth showed the minimum liftoff heights ( $\approx 50\%$  of the Reference case).

### 2.2.6 Velocity Fields Obtained from Stereo PIV

The six planes investigated in the stereo PIV measurements are illustrated in Fig. 9. Three planes (Pxy\_C, Pxy\_Q and Pxy\_H) were parallel to xy plane, where x was a coordinate parallel to the initial direction of methane jet injection, and y represented a spanwise coordinate (see Fig. 2). The other three (Pyz\_C, Pyz\_Q, and Pyz\_H) were parallel to yz plane. The Pxy\_C plane passed through the center of spanwise (S) cavities in the D+S or T+S geometries, and the Pxy\_Q and Pxy\_H planes were offset 0.25 inch and 0.5 inch from the center plane, respectively. Hence, the plane Pxy\_Q passed through the side wall of the S cavity, and Pxy\_H was located at the center of the no-cavity region. The planes Pyz\_C, Pyz\_Q, and Pyz\_H were located at the center of the bluff body, 0.25 inch from the center and 0.5 inch from the center, respectively. The Pyz\_H plane intersected the edge of the bluff body. Throughout this section, only the reference geometry, the D+S, and the T+S geometries with the lowest liftoff heights (see Fig. 8) were considered.

Figures 10a, b, and c show ensemble-averaged PIV images from 100 instantaneous snapshots for the Reference, D+S, and T+S geometries along the Pxy\_C plane, respectively. Figure 10d shows the corresponding centerline velocities along the y coordinate. The color coding in all the PIV images provided in this study represents the out-of-plane velocity component. For example, the red, green, and blue colors represent out-of (+z direction), within (in plane xy), and into-the-paper (-z direction) components of the velocities, respectively. The white lines are pseudo-streamlines obtained from in-plane velocity components.

As shown in Figs. 10a, 10b, and 10c, xy-plane recirculation regions were present in all three cases, as expected; however, noticeable differences in terms of location of vortices and the strength of the recirculation in the vicinity of the bluff body were observed among the three



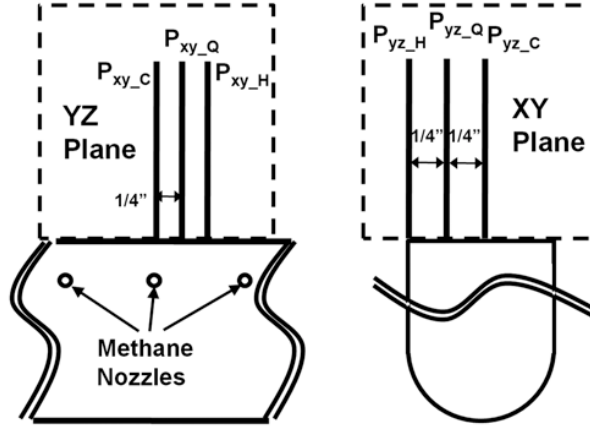


Figure 9: Schematic of the six planes of interest in the PIV measurements.

cases. The center of vortices (denoted by  $\omega_z1$  in this study) were further away from the bluff body in the case of the Reference ( $\approx 23$  mm from the base) compared to that of the D+S ( $\approx 14$  mm) and the T+S ( $\approx 5$  mm) cases. Furthermore, the minimum vertical velocity in Fig. 10d was significantly higher for the Reference geometry (dashed line,  $\approx 0.1$  m/s) than that of the D+S (dotted line,  $\approx -0.6$  m/s) and the T+S (solid line,  $\approx -0.8$  m/s) geometries. These facts showed that the small distance of the vortices from the bluff body and the intense near-base recirculation in the D+S and T+S geometries caused the reductions in liftoff heights.

The recirculating regions of all three cases generally shared common features for the out-of-plane velocity component ( $w$ ) in the  $xy$  plane, which are represented by the yellow or red color in the recirculation regions of Figs. 10a, 10b, and 10c. These biased out-of-plane velocities most likely were generated due to the imperfect symmetry in the current experiment. The postulated reason for the out-of-plane velocities was even more plausible when one considered the study by Smith & Mungal (1998) in which they showed that a single jet in crossflow leads to asymmetric development downstream. Thus, it would be difficult to have six such jets interacting with the bluff body base and produced a perfectly symmetric flow (the asymmetry was observed more clearly in the  $yz$  plane PIV measurements, which will be discussed below). A more careful inspection of the results in Fig. 10 revealed that the  $w$  component in the recirculation region of the D+S cavity showed noticeable gradients along both the  $y$  coordinate (from the pale blue at the bottom to the red at  $y \approx 16$  mm) and the  $x$  coordinate (from the red at the center to the blue at  $x \approx \pm 5$  mm) compared to the Reference case (constant yellow). These gradients implied that there existed out-of-plane vortical motions (denoted by  $\omega_x1$  and  $\omega_y1$  in directions  $y$  and  $x$ , respectively and depicted in Fig. 10b by thick white lines) in the D+S cavity, which was one of the key elements for decreasing liftoff height reported in this study. Those vortices might also be present for the T+S case, but they were not detected. The plane Pxy\_C was located significantly further from the top of the S cavity portion in the T+S geometry than in the D+S geometry, which resulted in lower strength of the significant vortical motions.

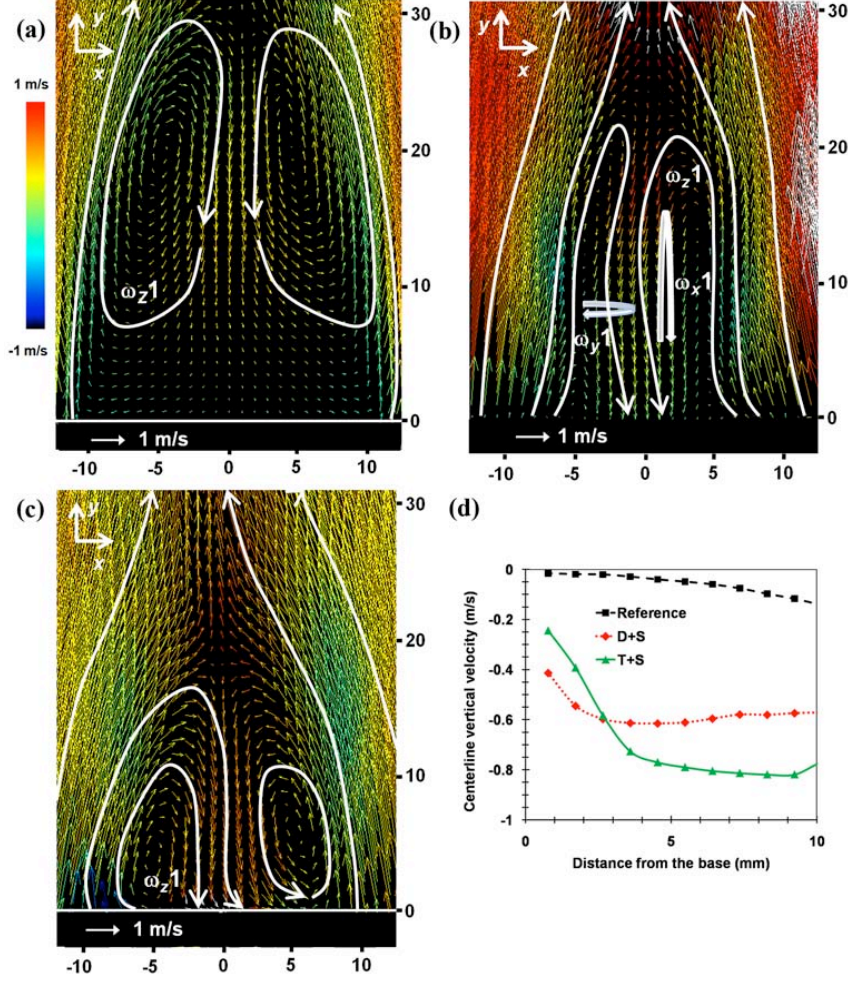


Figure 10: Ensemble averaged PIV images of (a) the Reference, (b) the D+S, and the (c) T+S geometries in the Pxy-C, and (d) corresponding centerline velocities along the y coordinate. The color coding represents out-of-plane velocity component, while the white lines show the pseudo streamlines and the sketches of vortices.

Figures 11a and 11b show the ensemble-averaged PIV images in the plane  $P_{xy\_Q}$  of the D+S and the T+S geometries, respectively. Experimental conditions were identical to those of Fig. 10 except that the plane of interest was offset by 0.25 inch such that the laser sheet illuminated the boundary of the cavity and no-cavity regions. Compared to the reference center plane ( $P_{xy\_C}$ ), the flow patterns were significantly different qualitatively in the current plane for the D+S cavity than those observed for the T+S cavity. For the D+S cavity, the strong recirculating flow along the negative y-direction was diminished, and more intense x-directional flow was observed. This x-directional motion also was confirmed by a subsequent tuft flow visualization in a non-reacting environment, where a single tuft was placed at the end of a long slender rod to probe the base flow. In accordance with the tuft visualization experiment, there existed significant flow motion from one S cavity to the adjacent (or oppositely located) S cavities through the D cavity inside. The x-directional flow detected here, therefore, was a consequence of the cavity-cavity flow. For the w velocity component in this geometry, more intense (bright red) outward (+z direction) flow was observed in the current plane compared with that of the center plane. This high flow intensity was caused by i) the current plane located at the boundary of the cavity and the no-cavity regions was intrinsically asymmetric and ii) there existed additional inter-cavity flows, from one cavity to the adjacent cavities on the same side. The more intense outward flow in this plane also was observed in the T+S geometry, as shown in Fig. 11b; however, no other noticeable difference in the flow pattern was observed for the T+S geometry in the current plane compared with that in the center plane.

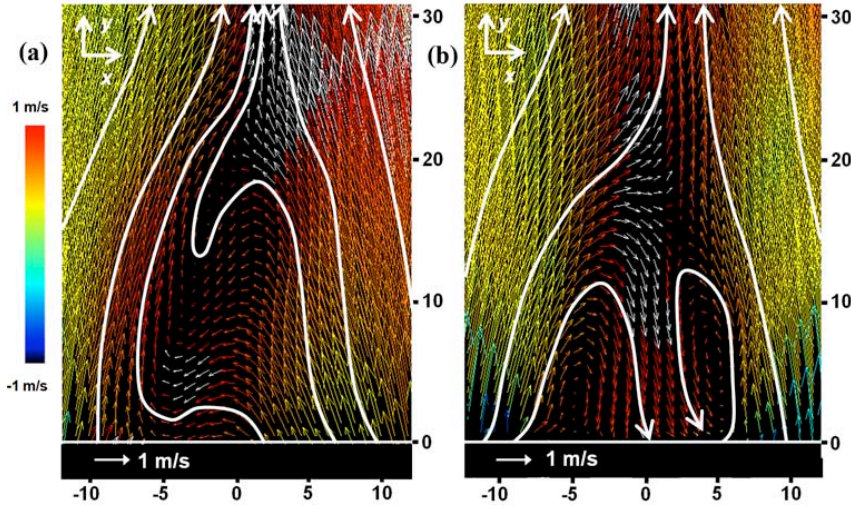


Figure 11: Ensemble averaged PIV images of (a) the D+S and (b) the T+S geometries in the  $P_{xy\_Q}$ .

Figures 12a and 12b show the PIV images at the center of the no-cavity regions (Plane  $P_{xy\_H}$ ) of the D+S and the T+S geometries, respectively, under flow conditions identical to those of Fig. 10. In the D+S cavity case, the width of the recirculation region of the D+S

cavity in the current plane was noticeably larger compared to that in the plane Pxy\_C shown in Fig. 10b. The larger recirculation was observed because the stream in the current plane did not experience the slender S cavity portion but instead flowed through the wider no-cavity region. All other flow features in this plane for the D+S case were similar to those observed in Fig. 10b, such as i) the intense near-base recirculation, ii) the presence of the  $\omega_x1$  and  $\omega_y1$  (observed from the gradient of color coding along the y and x coordinates, respectively), as well as  $\omega_z1$ . A more detailed inspection, however, showed that there existed quantitative differences between the flow fields of the center plane (plane Pxy\_C) and the current plane, e.g., the location of  $\omega_z1$  ( $\approx 20$  mm) in the current plane was higher ( $\approx 15$  mm). Also, the centerline velocity along the y coordinate of the current plane was  $\approx 20\%$  smaller than that observed in the plane Pxy\_C.

These differences also were observed in the case of the T+S geometry (Fig. 12b). For the T+S geometry, the location of  $\omega_z1$  was higher ( $\approx 10 - 13$  mm) than that of the center plane ( $\approx 5$  mm), and the centerline velocity in the current plane was reduced by 30 % (not shown) in comparison with that of the center plane. We believed that the higher location of  $\omega_z1$  and the reduced strength of the recirculating flow were partially responsible for the higher liftoff height in the case of out-of-phase nozzle placement corresponding to the nozzle geometry described in Fig. 7b.

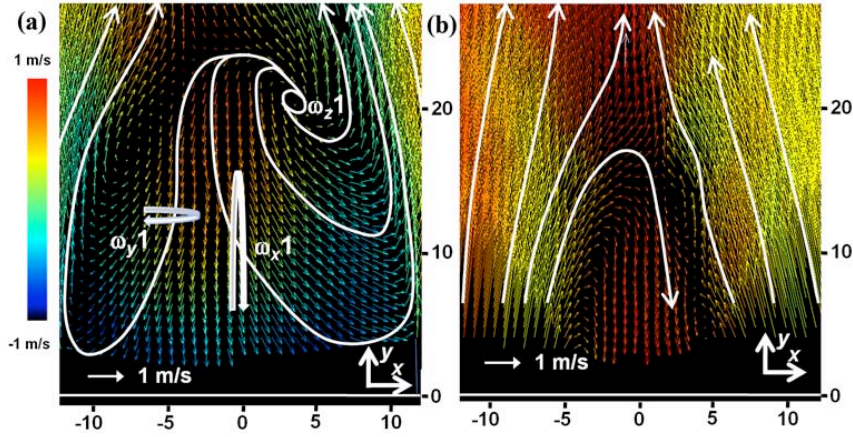


Figure 12: Ensemble averaged PIV images of (a) the D+S and (b) the T+S geometries in the Pxy\_H.

Figure 13 shows the ensemble-averaged PIV images of the Reference case (Fig. 13a), the D+S cavity (Fig. 13b), and the T+S (Fig. 13c) geometry for the plane Pyz\_H, which was offset from the center plane (yz plane) by 1/2 inch. The red and blue colors represent the outward fluid motion ( $-x$  direction for the current plane) and inward motion ( $+x$  direction), respectively. As expected, most of the in-plane (yz plane) velocity vectors uniformly pointed downstream in all three cases since this plane was very close to the freestream. With a careful investigation of the color coding, one could find the presence of the  $\omega_z1$  (observed in Figs. 10 and 12) for the Reference and the D+S geometries from their upstream yellow color and their



blue color downstream. Another observation from the color coding was that the outward flow in the vicinity of the no-cavity, and also inward flow in the vicinity of the cavity, of the D+S geometry was noticeable, unlike the Reference geometry. This inward/outward flow was because the cavity region of the D+S cavity geometry was retarded by 0.4 inch from the no-cavity region. The presence of the out-of-plane velocity also was found in the T+S geometry, which could be confirmed from the color coding gradients in Fig. 13c. More significant inward flow (deep blue or black) was observed in the no-cavity region downstream of the T+S in comparison to that in the cavity region, which was opposite to the D+S case. This significant inward flow was because the no-cavity surface of the T+S is  $25^\circ$  slanted backward from the current PIV plane, while the back surface of the S cavity was parallel to the plane, which mitigated an intense inward flow at the cavity downstream.

The ensemble-averaged PIV images in the plane  $\text{Pyz.Q}$  are shown in Fig. 14. Unlike for the previous plane, the overall flow pattern of this plane did not point in the  $+y$  direction, but was biased to the right. This asymmetry probably was caused by i) a slight misalignment between the burner and the bluff body, ii) the complicated interaction between the crossflow and the methane jet (Smith and Mungal 1998), and iii) possible asymmetric suction flow along the  $z$  direction at the edges of the bluff body due to the influence of the shear layers formed by the speed difference between the post combustion gas ( $\approx 5$  m/s) and the surrounding non-reacting air stream ( $\approx 3.5$  m/s). This observation was consistent with the red shift observed in Fig. 10. The typical speeds of the biased flow measured in this plane were quite small,  $\approx 0.03$  m/s, for the Reference case and somewhat larger,  $\approx 0.3$  m/s, for the cavity cases.

For the Reference geometry (Fig. 14a), the presence of the  $\omega_z 1$  observed in the previous planes was seen more clearly from the upstream yellow color coding with the subsequent downstream blue. Also, the low downward flow speed (flow along  $-y$  direction) confirmed the previous observations shown in Fig. 10a. For the D+S geometry shown in Fig. 14b, a more complex flow field due to the inward (yellow) and outward (blue) flows in the vicinity of the cavity and no-cavity regions, respectively, was seen more clearly. Also, this geometry had vortices along all three coordinates. Along the  $x$  coordinate, the  $\omega_x 1$  was present at the left bottom corner of the figure, which resulted in a strong recirculation into the cavity region. Furthermore, one could find that another set of in-plane vortices (so called,  $\omega_x 2$ ), located slightly lower than  $\omega_x 1$  (see the figure for its location), was present, probably induced by a back step formed by the side surface of the S cavity and the bottom surface of the D cavity. Along the  $z$  coordinate, the  $\omega_z 1$  was present as could be conjectured from the yellow no-cavity region upstream and the blue region downstream. Along the  $y$  coordinate the presence of the  $\omega_y 1$  swirling motion from a cavity to the left corner of the adjacent cavity on its right could be found also from a careful examination of the color coding (see the sketch in Fig. 14b). In general, we believed that these multiple, three dimensional small scale, coherent vortices due to the presence of the D and the S cavities mutually dissipated one another. As a result, these vortices played a central role in decreasing the liftoff height, especially in comparison with the Reference case, which only

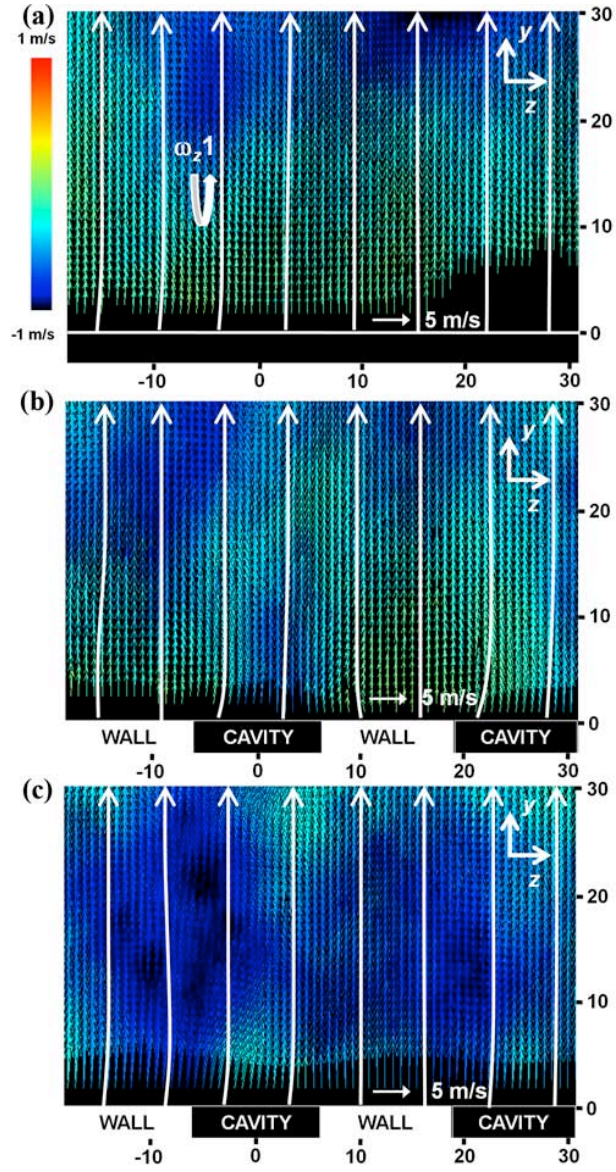


Figure 13: Ensemble averaged PIV images of (a) the Reference, (b) the D+S and (c) the T+S geometries in the Pyz\_H.

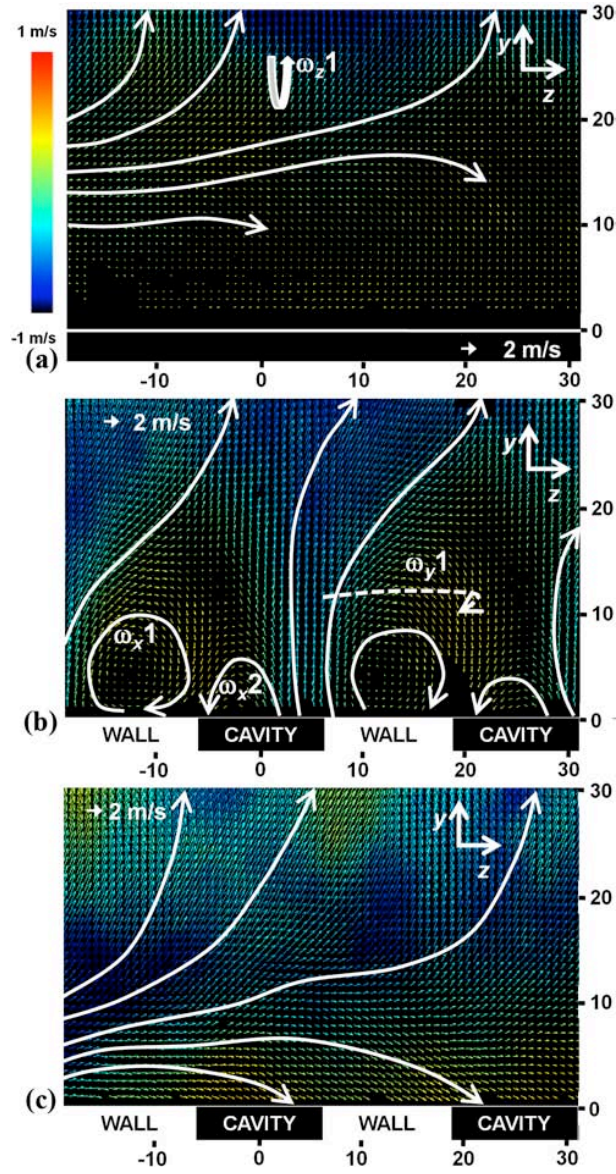


Figure 14: Ensemble averaged PIV images of (a) the Reference, (b) the D+S and (c) the T+S geometries in the Pyz-Q.

had the coherent vortex,  $\omega_z 1$ . These three-dimensional vortical structures might be expected in the T+S geometry (Fig. 14c), but they were not seen clearly in the current plane, which was probably due to the longer distance between the S cavity and the plane of interest.

In Fig. 15, ensemble-averaged PIV images in the yz center plane (P<sub>yz</sub>-C) of the Reference (Fig. 15a), the D+S (Fig. 15b), and the T+S (Fig. 15c) geometries are shown. Again, the fluid motions in the recirculation zone ( $y \approx 7 - 30$  mm for the Reference,  $\approx 7 - 22$  mm for the D+S, and  $\approx 7 - 15$  mm for the T+S) of all three cases generally pointed to the right (+z direction) of the image, which was consistent with Fig. 14. Also, other flow patterns observed in the previous planes could be confirmed in this plane. For example, the Reference had a relatively organized color coding pattern, a yellow colored band  $7 - 17$  mm and a subsequent blue colored band more downstream, which corresponded to the  $\omega_z 1$  vorticity. The complex flow pattern in the D+S cavity was shown too, e.g., i) outward (yellow) and inward (blue) flows observed in the vicinity of the no-cavity and the cavity regions, respectively, ii) the presence of in-plane (yz plane) vortices in the vicinity of the boundary of the cavity/no-cavity regions as a consequence of  $\omega_x 1$ , and, as a result, iii) intense downward flows induced from the no-cavity to the cavity regions, especially at a height of  $7 - 15$  mm, which was represented as the intense y-directional downward flow in Fig. 10. Again, it appeared that the intense recirculating flows of this geometry assisted in the decrease of the liftoff height by promoting localized, but adequate, mixing between the cavity flow (primarily fuel) and no-cavity flow (primarily air), which was beneficial in holding the downstream lifted jet flame. In the case of the T+S geometry, one still could find the downwards in-plane flows to the cavity region ( $7 - 12$  mm height) probably due to the  $\omega_x 1$  (not shown in the current region of interest); however, the out-of-plane (x coordinate) flow motion of this geometry, seen from the color coding, seemed somewhat less-correlated with the cavity locations than that observed in the D+S cavity. Again, the less correlated out-of-plane flow pattern seemed to be caused by the longer inter-distance between the S cavity portion of the T+S geometry and the current plane P<sub>xy</sub>-C, and, as a result, the effect of the S cavity was diminished.

### 2.2.7 Vorticity and Strain Rate Fields

The mean vorticity and mean strain rates are shown in Figs. 16 and 17, respectively. These fields were presented for three cases, Reference, D+S and T+S, in the xy (Figs. 16a and 17a) and in the yz planes (Figs. 16b and 17b). Both the strain and vorticity fields exhibited similar characteristics in the planes reported. In the xy plane, the strain and vorticity were more diffused close to the body for the modified geometries. In the yz plane, the high shear and vortical regions of the flow were observed to emanate from the spanwise geometrical variations and most likely played a role in the mean flame behavior. The vortical patterns will be discussed further in the next section.



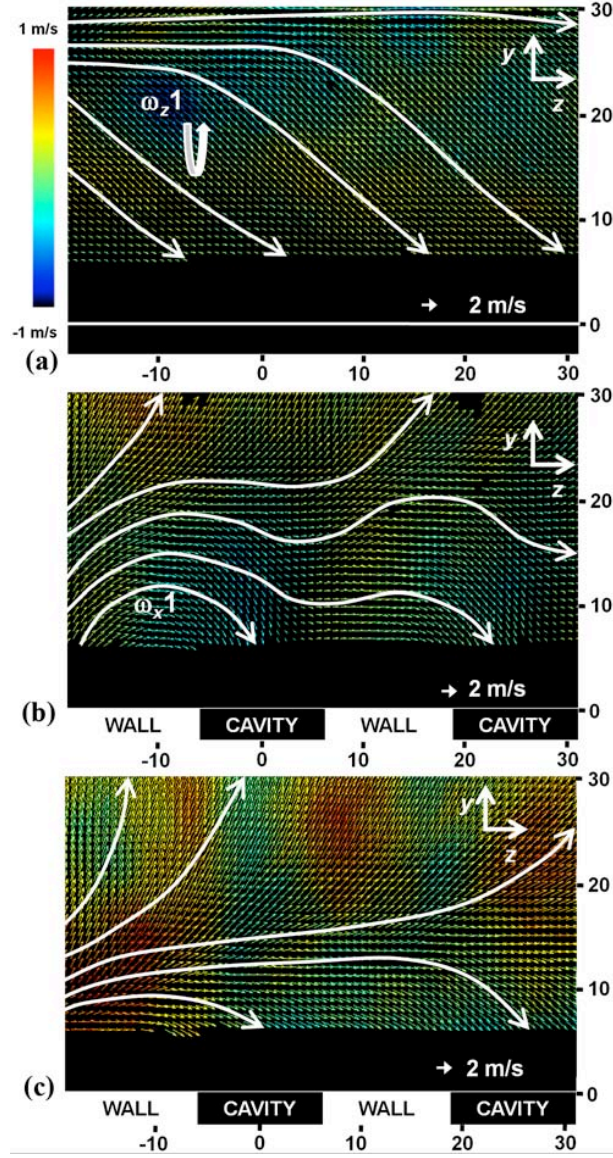


Figure 15: Ensemble averaged PIV images of (a) Reference, (b) D+S and (c) T+S geometries in the Pyz\_C.

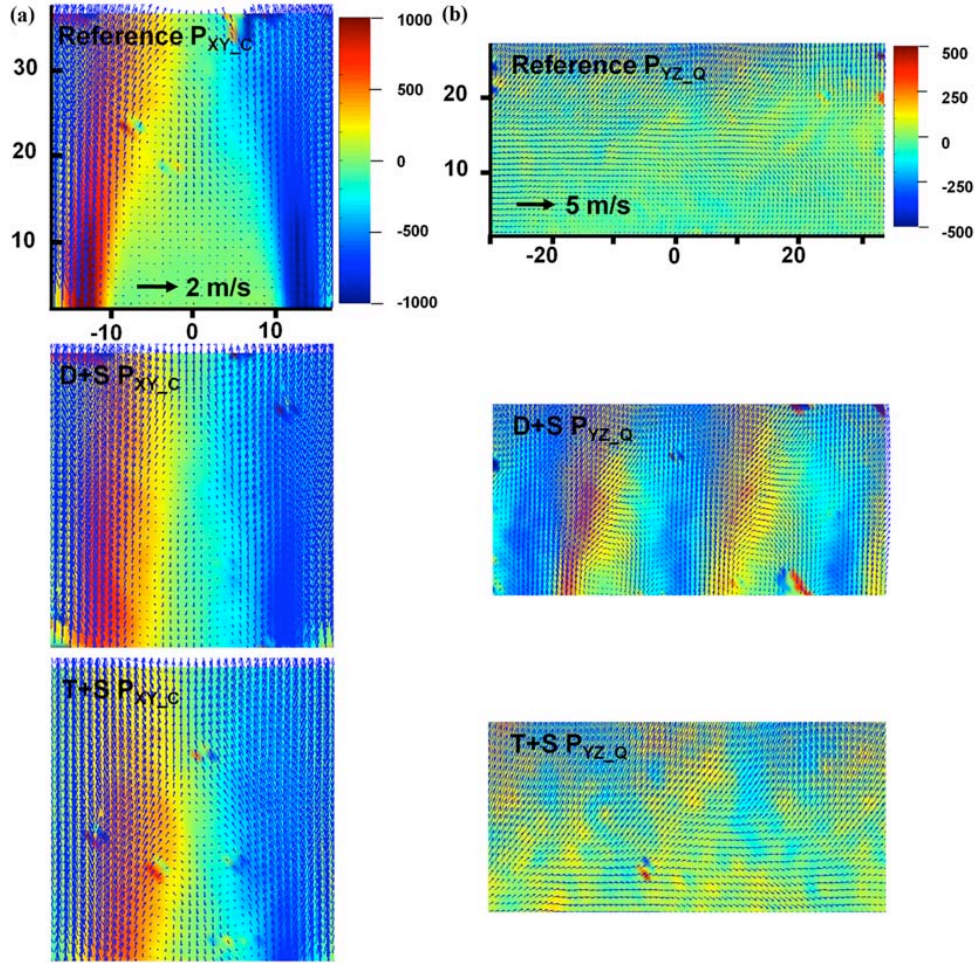


Figure 16: Mean vorticity fields of Reference, D+S, and T+S geometries in planes (a)  $P_{xy\_C}$  (b)  $P_{yz\_Q}$ .

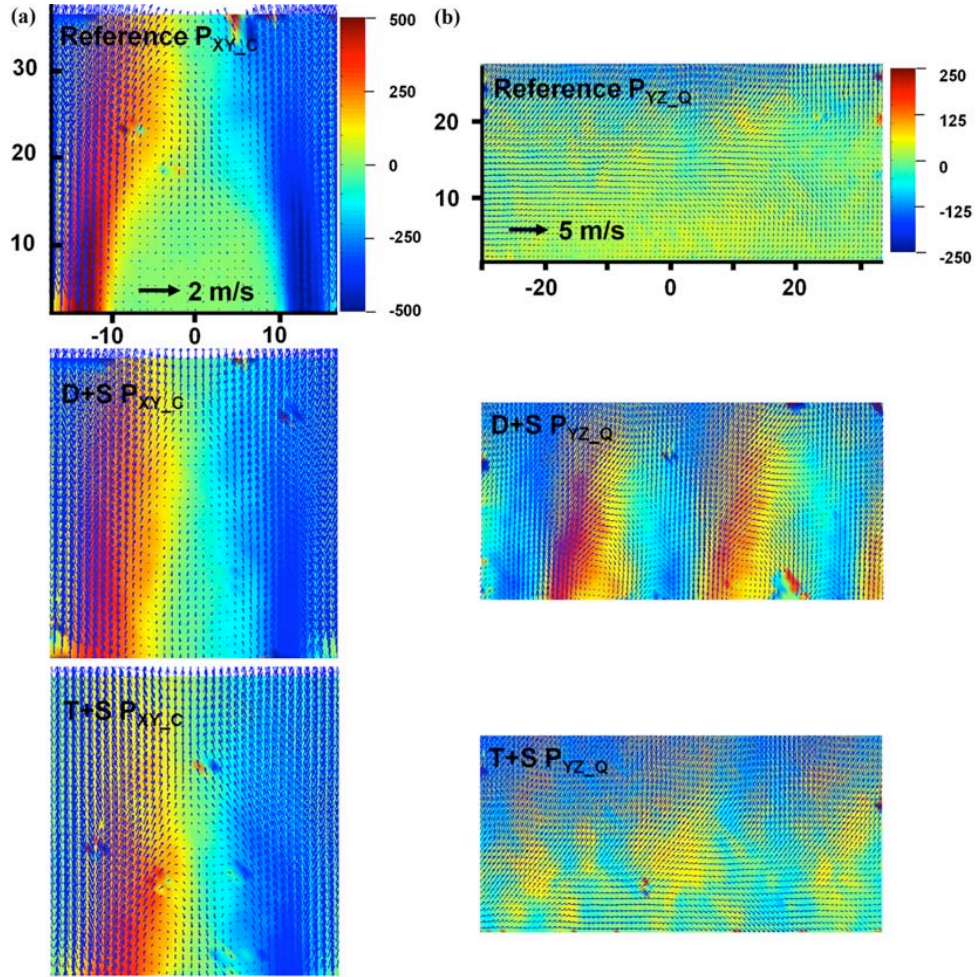


Figure 17: Mean strain rate fields of Reference, D+S, and T+S geometries in planes (a)  $P_{xy\_C}$  (b)  $P_{yz\_Q}$ .

### 2.2.8 Summarizing Schematics of Flow Patterns with Local Cavity Geometries

This section summarizes the flow patterns observed thus far. The flow field schematics in the vicinity of the three geometries are provided in Fig. 18. The flow schematic in the bluff body downstream of Fig. 18 was constructed using the PIV results presented in the previous section, whereas the flow inside the cavities was conjectured based on a subsequent visualization of a tuft flow experiment in a non-reacting environment.

As shown in Fig. 18a, there exists only one vortex pair,  $\omega_z1$ , in the Reference geometry. For an ideally symmetric experiment, this large scale vortex would share identical shedding frequency with adjacent vortex pairs along the  $z$  coordinate, which did not seem beneficial for improving flame stability (Kurimoto *et al.* (2004); Paschereit *et al.* (2006))

In contrast, multi-dimensional vortical structures were formed along the  $z$ ,  $x$ , and  $y$  coordinates in both D+S and T+S geometries (Figs. 18b and 18c, respectively). In the case of the D+S, aside from  $\omega_z1$ , two additional  $z$ -coordinate vortical structures were observed: (a)  $\omega_z2$ , induced by a back step formed between the S-cavity back surface and the D-cavity bottom surface, and (b)  $\omega_z3$ , induced by the back step formed by the bluff body side surface and the S-cavity bottom surface. These vortices had different shedding locations and frequencies due to the difference in effective height and thickness of the local geometry from which each vortex was generated. The different shedding characteristics might lead to the mutual dissipation of coherent vortical structures, which eventually might result in higher flame stability.

Along the  $x$ -coordinate, two vortical structures,  $\omega_x1$  and  $\omega_x2$ , also were formed: by the back steps with the side surface of the S cavity and the top surface of the no-cavity region ( $\omega_x1$ ), and the side surface of the S cavity and the bottom surface of the D cavity ( $\omega_x2$ ), respectively. We believed that these vortices, along with the  $\omega_z2$ , were essential to mixing between fuel that flowed through the S cavity region and air, which flowed along the no-cavity region ( $\omega_x1$ ) or resided inside of the D cavity ( $\omega_x2$  and  $\omega_z2$ ).

Finally, a vortical structure along the  $y$ -coordinate,  $\omega_y1$ , was also present, as previously confirmed in Figs. 10 and 14. This vortex was produced by an inter-cavity flow that started from one of the S cavities, passed through the inside of the D cavity, and finally exited to the left corner of the adjacent cavity on its right. As a result, the flow produced a swirling motion surrounding the no-cavity region. The swirling motion was clockwise when seen from the top, and, therefore, the resulting vortex pointed in the  $-y$  direction. We believed that its companion vortex (pointing in the  $+y$  direction) should be present if ideal symmetry could be achieved.

For the T+S geometry, a large vortex due to the slanted side surface of the T geometry ( $\omega_z1$ ), a small vortex due to the back step formed by the side surface of the bluff body and the bottom surface of the S cavity ( $\omega_z3$ ), and a mid-size vortex due to the back step formed by the back surface of the S cavity and the slanted T surface ( $\omega_z2$ ) were present. An additional vortex ( $\omega_x1$ ) was present in this geometry along the  $x$  coordinate due to the back step formed by the side surfaces of the S cavity and the slanted T surface. This vortex induced inter-cavity flow along the slanted T surface observed in Figs. 14 and 15. Again, these multiple vortices had



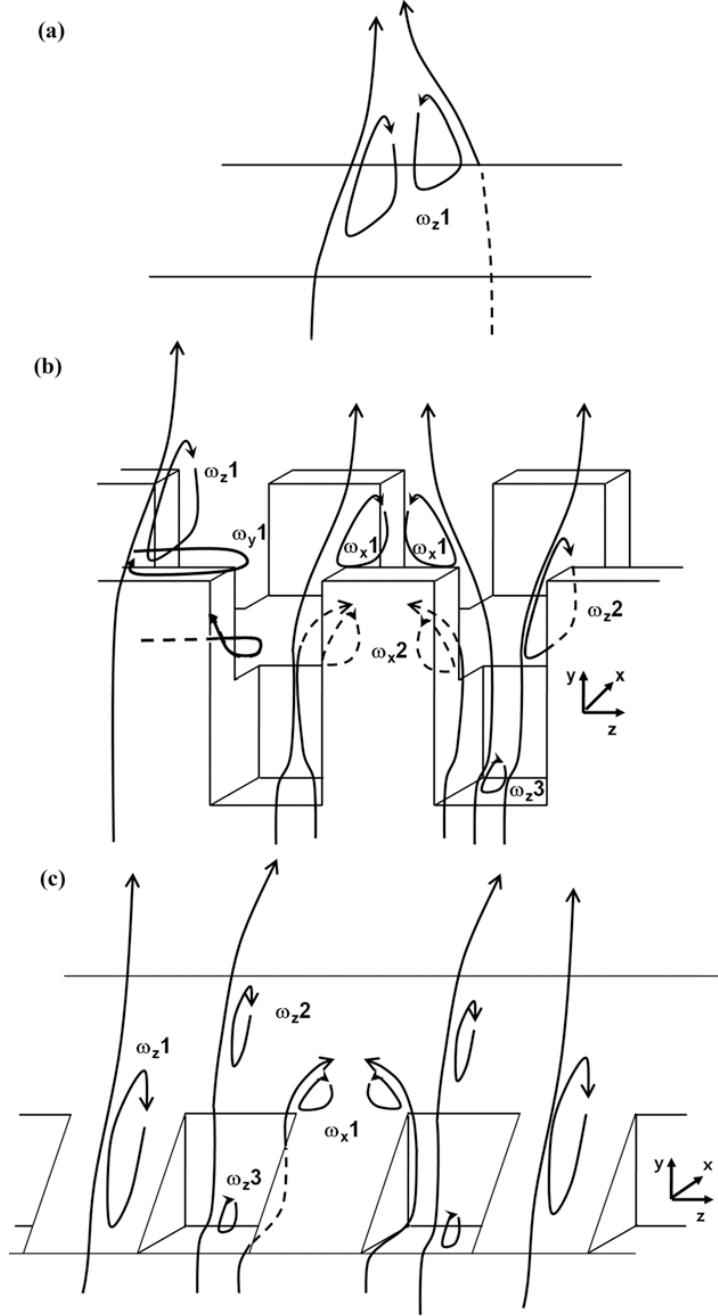


Figure 18: Overall flow pattern of (a) the Reference, (b) the D+S and (c) the T+S geometries.

different shedding frequencies and locations.

## 2.3 Blowout Study

Here, we present variations of the flame configuration to study blowout effects. In this section, our discussion will be limited to the six base geometries: R, D, T, R+S, D+S, and T+S shown in Fig. 4. The results from these selected geometries would show the significance of the S cavity.

### 2.3.1 Variation of Flame Configuration

Three flame configurations were considered: i) a fully premixed freestream stabilized by a bluff body (fully premixed mode); ii) an air freestream in which fuel was discharged from the bluff body (partially premixed mode); and iii) a combination of these two, namely a fully premixed freestream with additional fuel discharged from the bluff body. The premixed burner that was used to provide the vitiated air flow in the liftoff study also was used here to supply a fully premixed (for fully premixed and hybrid modes) or pure air (for partially premixed mode) stream at room temperature.

### 2.3.2 Gas Chromatography for Measuring Methane Concentration

Gas chromatographic measurement was performed to quantify the local methane concentration in the vicinity of the bluff body base using a Varian 3400 Gas Chromatograph equipped with Porapak Q (for nitrogen and oxygen) and Molecular Sieve 5A (for methane) as columns and a thermal conductivity detector (TCD). All sampling measurements were conducted in the absence of the flame. For the sampling the spatial scanning was carried out by three translation stages (along the x, y, and z coordinates) using a  $\approx 1$  mm diameter (ID), 200 mm long stainless steel probe.

### 2.3.3 Blowout Limit Measurements

Figure 19 shows the results obtained from the ensemble averaged flame blowout limit. These results were quantified in terms of the local flow speed measured at 2 cm distance away from the methane nozzle for all six cases discussed in Section 2.3.1 operating in the hybrid, fully premixed, and partially premixed conditions. To vary the local flow speed, additional air from the turbulent grid was injected, and its flowrate was varied (from 40 SLPM to 200 SLPM) until the entire bluff body stabilized flame, which was formed from the fully premixed flow from the gas blower and pure methane jet injected from the methane nozzle, was blown out. The equivalence ratio and the speed of the fully premixed stream from the gas blower were kept identical at 0.72 and  $\approx 0.83$  m/s, respectively. The amount of methane injection from the nozzle also was kept fixed at  $\approx 3$  SLPM such that the (nominal) square root of the momentum ratio ( $r$ ) calculated from the main fully premixed stream and the injected methane was  $\approx 1.2$  (the  $r$  parameter ranges from 0.2 to 0.9 when it was calculated based on the nominal local speed formed

by the main fully premixed flow and additional air injection). For the blowout experiments, the relative placement of the methane nozzle and the local cavity was in-phase.

The critical nominal flow speeds in the blowout limit (black solid bar in Fig. 19a) were as low as  $\approx 3.7$  m/s for R,  $\approx 3.7$  m/s for D, and  $\approx 4.7$  m/s for T geometries, which did not include any cavity. The critical speed was improved significantly by adding local cavities to the original geometries; i.e., by 48 % for the R+S geometry, by 42 % for the D+S geometry, and by 10 % for the T+S geometry. The difference between the T and T+S geometries was small, which probably was due to the fact that i) the T geometry already showed a good capability to extend the blowout limit in comparison with those of R and D and ii) the size of the S cavity on the T geometry was small (due to slanted side surface of T), and, therefore, the effect of the S cavity was relatively weaker. The identical experiments without the injection of pure methane (fully premixed mode), denoted by the shaded bars in Fig. 19a, showed no apparent stability enhancement with addition of the S cavity. This observation, i.e., minimal positive effect on blowout limit extension with the geometrical change of bluff body, was consistent with previously published results (Stwalley & Lefebvre (1988) and Khosla *et al.* (2007)). For comparison, we also carried out an experiment that is similar, but with methane injection into pure air crossflow (partially premixed mode). As shown in the dotted bar, no significant extension of the blowout limit was observed among the various geometries.

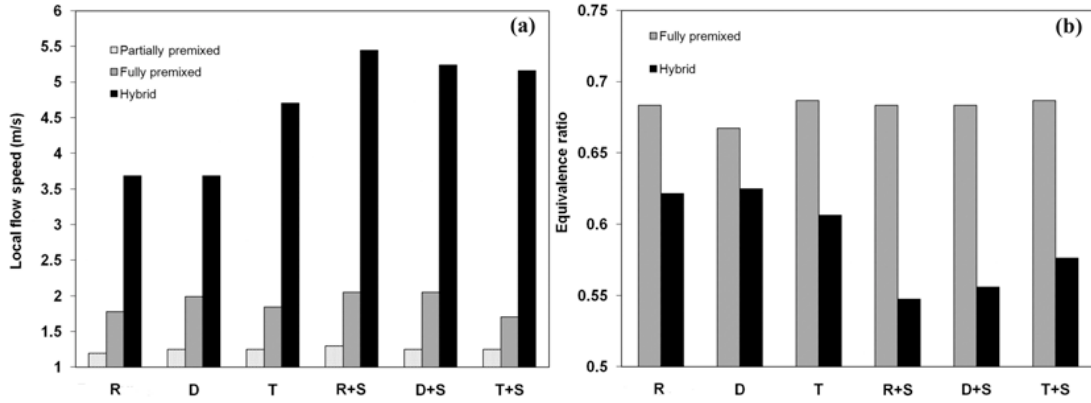


Figure 19: Blowout limits in terms of (a) local flow speed (measured at 2 cm horizontal distance from the methane nozzle) and (b) equivalence ratio of fully premixed stream for various bluff body base designs. For (a), the equivalence ratio of the fully premixed stream was kept fixed as 0.72 (for the fully premixed and hybrid modes) whereas in (b) nominal local flow speeds of were kept identical to 1.5 m/s (fully premixed mode) and 2.8 m/s (hybrid mode).

In Fig. 19b, the blowout limits in terms of equivalence ratio (of the fully premixed main stream) for all six geometries are plotted. The injected air rates (from the turbulent grid) were kept fixed at  $\approx 50$  SLPM (in the fully premixed case) and  $\approx 100$  SLPM (in the hybrid case), respectively. The blowout limit was measured by gradually decreasing the injected methane

rate in the fully premixed stream until no bluff body-stabilized flame was present while the air flowrate of the stream was kept identical at  $\approx 1720$  SLPM. The resulting nominal flow speeds of the stream were 1.5 m/s and 2.8 m/s for the fully premixed mode and the hybrid mode, respectively.

In the hybrid mode (black solid bar), the presence of the local cavity in the R+S, D+S, and T+S geometries extended the blowout limit from 0.62 (R and D) and 0.61 (T) to 0.55 (R+S), 0.56 (D+S) and 0.58 (T+S). This trend was consistent with what was observed in Fig. 19a. Again, for the fully premixed mode (shaded bar), no significant dependence of the blowout limits on the geometries tested was observed, which also confirmed the previous observation in Fig. 19a. Thus Figs. 19a and 19b suggested that there were no clear benefits to blowout limits in both the fully premixed and partially premixed modes of operation, but there were clear benefits in the hybrid mode of operation. The fully premixed results were consistent with observations of Stwalley & Lefebvre (1988) and might suggest that the presence of large-scale oscillations was not an indication of blowout and that this phenomenon was more likely related to the observations of Shin & Ferziger (1991).

### 2.3.4 Measurements of Methane Mole Fraction Field

Figures 20a and 20b show the variation of methane mole fraction along the  $y$  and  $z$  coordinates in the non-burning hybrid mode case, respectively. For all of these mole fraction measurements, the equivalence ratio and the speed of the fully premixed stream were kept fixed as 0.72 and 0.83 m/s, respectively. The flowrate of the additional air injection also was kept constant at 100 SLPM. The resulting speed, including the air injection (measured at  $x \approx 20$  mm), was  $\approx 3$  m/s. The measurements in Fig. 20a were taken at  $x = 0$  mm, the center of bluff body in the  $xy$  plane, and  $z = 0$  mm, the center of local cavity in the  $yz$  plane. The measurements in Fig. 20b are taken at  $x = 8$  mm and  $y = 6.5$  mm, from the top surface of the bluff body.

Along the  $y$  coordinate (Fig. 20a), the methane mole fractions of the non-local cavity geometries, especially R and D, were generally lower by  $\approx 50\%$  compared to those of the local cavity geometries (R+S, D+S and T+S) at least up to  $y = 1D$ , where  $D$  was the width of the bluff body (1 inch). We believed that the high fuel mole fractions, especially in the vicinity of the base, played an important role in increasing the flame stability for the local cavity geometries. We expected that the most active interactions between the base geometry and the flow would occur in the vicinity of the base. The results showed that the presence of the local cavity prevented the pure methane stream from being diluted excessively for which the partially premixed stream effectively could pilot the fully premixed stream. The T geometry showed a mole fraction field as high as those of local cavity geometries. This high mole fraction was clear in the PIV results (see Fig. 21 for the detailed flow field), which indicated the presence of a skewed flow along the slanted side surface of the T geometry. We believed that the skewed flow effectively could deliver the pure methane stream, especially at this low value of  $r$  ( $r < 1$ ), to the region investigated here such that the overall fuel mixture fraction in that region remained high.



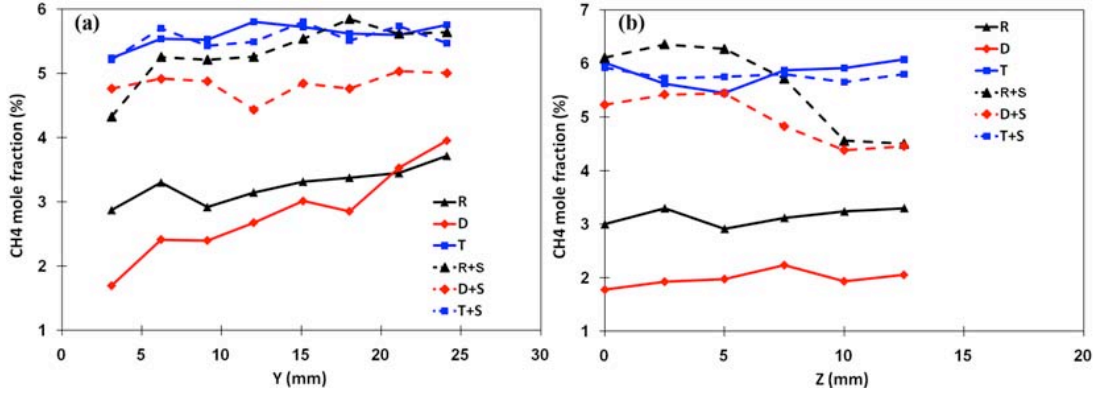


Figure 20: Methane mole fractions along the (a)  $y$  and (b)  $z$  directions for the six modified geometries. The equivalence ratio of the fully premixed stream was kept fixed as 0.72. The flowrate of the additional air injection also was kept at 100 SLPM such that the resulting nominal flow speed measured at 2 cm distance from methane nozzle was  $\approx 3$  m/s. Measurement locations were  $x = 0$  and  $z = 0$  for (a) and  $x = 8$  mm and  $y = 6.5$  mm for (b).

Figure 20b shows results of the same experiment, as described in the preceding paragraph, but along the  $z$  coordinate. From the figure, a similar trend existed, i.e., the local cavity geometries (and the T geometry) contained approximately two times higher local fuel mole fraction compared with the non-local cavity geometries (especially R and D). The mole fractions of R+S (black dotted line) and D+S (red dotted line) geometries decreased with increasing  $z$ , while the other four geometries showed a relatively invariant tendency of mole fraction along the  $z$  direction. The decay was more apparent when  $z$  was greater than  $\approx 6$  mm. This decay was because the local cavity section ended, and the wall section started from  $z = 6.4$  mm in those two geometries, which confirmed that the local cavity acted as an effective conduit of less diluted fuels. To study the capability of local cavity placement relative to the methane jet to localize the fuel stream further, we briefly investigated the blowout limit dependence (under experimental conditions of Fig. 20) on the location of the cavity relative to the methane jet nozzles. The result showed that the blowout limit for out-of-phase placement (i.e. the case that the center of the wall section was aligned with the methane nozzle) was  $\approx 20\%$  (in terms of the local flow speed) or  $\approx 7\%$  (in terms of the equivalence ratio of fully premixed stream) worse than those of in phase placement (i.e., the case where the center of the cavity section was aligned with the methane nozzle) for both the R+S and D+S geometries.

It was important to compare the mole fraction and velocity fields simultaneously. The total amount of fuel injection was identical for all the studied geometries, and, therefore, the lower methane mole fraction for non-local cavity geometries implied that there were regions of higher mole fraction (see Fig. 20). Hence, we believed that the distribution of the fuel mole fraction in the flow field was likely more important than the absolute value of the fuel mole fraction (shown in Fig. 20) itself. To investigate the mole fraction distribution resulting from

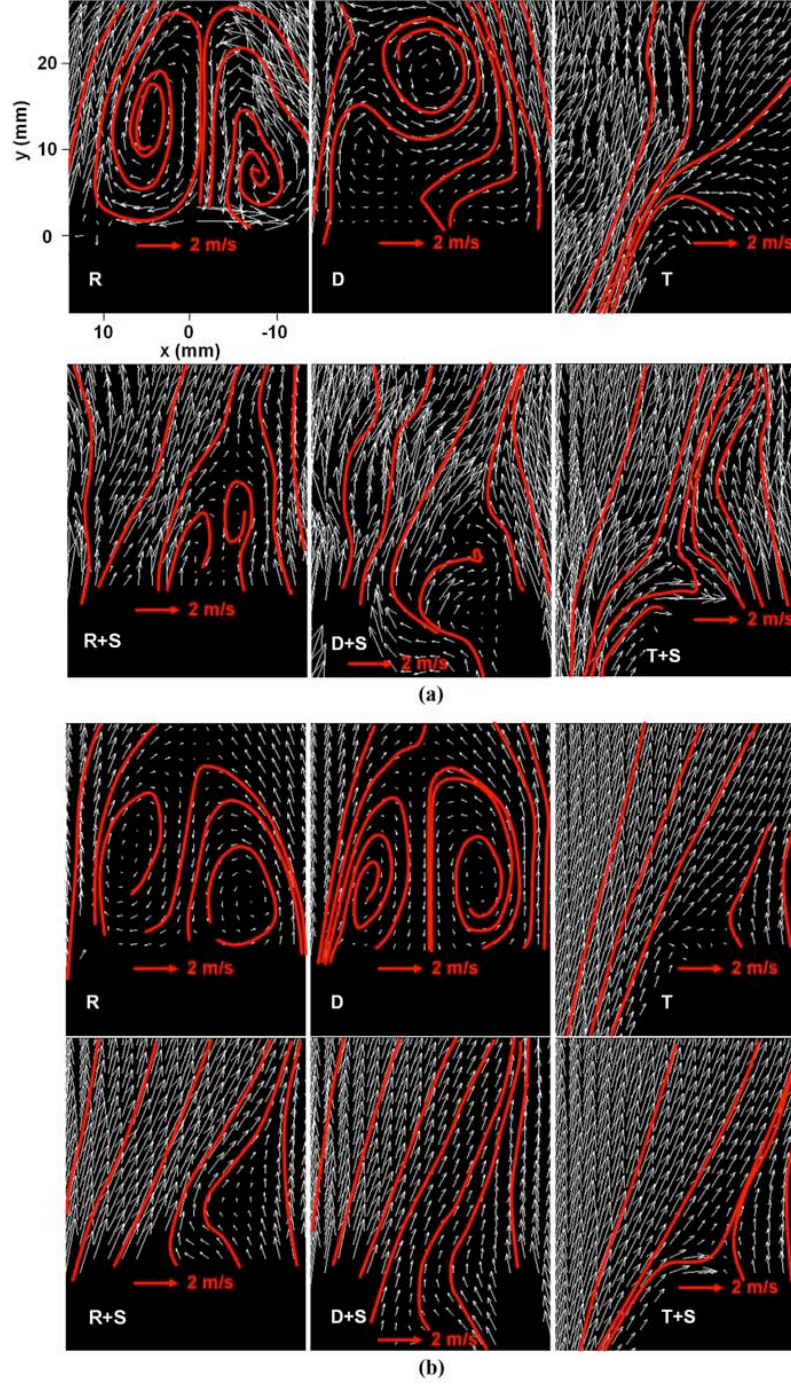


Figure 21: (a) Instantaneous and (b) ensemble averaged PIV images of the R, D, T, R+S, D+S, and T+S geometries. The nominal flow speed was  $\approx 3$  m/s and the equivalence ratio of the fully premixed stream was kept fixed as 0.72 for all images. The red lines represent the pseudo streamlines.

different flow fields, we carried out gas chromatographic sampling in parallel to independent PIV measurements. The gas chromatographic sampling results are shown in Fig. 22. In this figure, the variations of methane mole fraction along the  $x$  coordinate (at  $y = 6.5$  mm and  $z = 0$  mm) were plotted together with velocity components,  $V_x$  and  $V_y$ , at the equivalent locations of the gas sampling for all the six geometries. Similar to the case in Fig. 20, both the sampling and PIV measurements were for the non-reacting case.

As shown in Fig. 22, for the R (Fig. 22a) and D geometries (Fig. 22b), fuel mole fractions were relatively low ( $\approx 1.8 - 3.3\%$ ) at  $x < \approx 10$  mm, where the  $V_x$  and  $V_y$  velocities were also very low ( $< \approx 0.1$  m/s), while the higher velocity ( $V_y \approx 3$  m/s) region showed higher fuel mole fraction ( $\approx 5.5\%$ ). This type of fuel distribution, i.e. high fuel concentration in a high velocity region and low fuel concentration in a low velocity region, was not the most efficient way to improve flame stability. To the contrary, for the local cavity geometries in Figs. 22d – 22f (R+S, D+S, and T+S, respectively), the high fuel mole fraction ( $\approx 5 - 7\%$ ) region was maintained in relatively low velocity regions ( $V_y \approx 1 - 2$  m/s,  $V_x \approx 0 - 1$  m/s), where  $x < \approx 10$  mm, whereas the mole fraction decreased in the high velocity region ( $x > \approx 15$  mm). For example, the region of peak mole fraction in the R+S geometry ( $x \approx 4$  mm) contained regions with velocities  $V_y \approx 2$  m/s (69% of peak  $V_y$ ) and  $V_x \approx 0.8$  m/s, whereas in the R geometry ( $x \approx 16$  mm) the velocities were  $V_y \approx 3$  m/s (99% of peak  $V_y$ ) and  $V_x \approx 0.1$  m/s.

An interesting observation could be made by looking at the gradients of fuel mole fraction. For the R and D geometries, the mole fractions increased by more than 100% (from  $\approx 2.5\%$  to  $\approx 6\%$ ) within  $\approx 4$ -mm distance, but for the local cavity geometries, the variations of the mole fraction were much smaller, less than 25% in the highest case. We believed that specific fuel distributions, as well as smaller mole fraction gradient in the presence of the local cavities, effectively improved blowout limits in the hybrid mode flow.

As a final comment on the results presented in Fig. 22, we compared the mole fraction and velocity fields of T (Fig. 22c) and T+S (Fig. 22f) geometries. The behavior of the two fields was generally similar for both geometries. Both cases showed a gradual decay of the mole fraction field from  $\approx 6\%$  to  $4.5\%$ , a gentle increase of  $V_y$  up to  $x \approx 12.5$  mm, and an asymptotic decrease to the free stream velocity with increasing  $x$ . As mentioned earlier, this similarity was caused by the fact that the size of the cavity in the T+S geometry was relatively small; however, one could still observe some evidence of the presence of the local cavity from the mole fraction data at  $x \approx 12$  mm in the T+S geometry (orange circle). The mole fraction of the T+S geometry was 10% higher than that of T, while the neighboring mole fractions (e.g., at  $x \approx 10$  mm and 14 mm) were almost identical for both geometries. We believed that the presented data further confirmed the capability of a local cavity to localize the fuel stream.

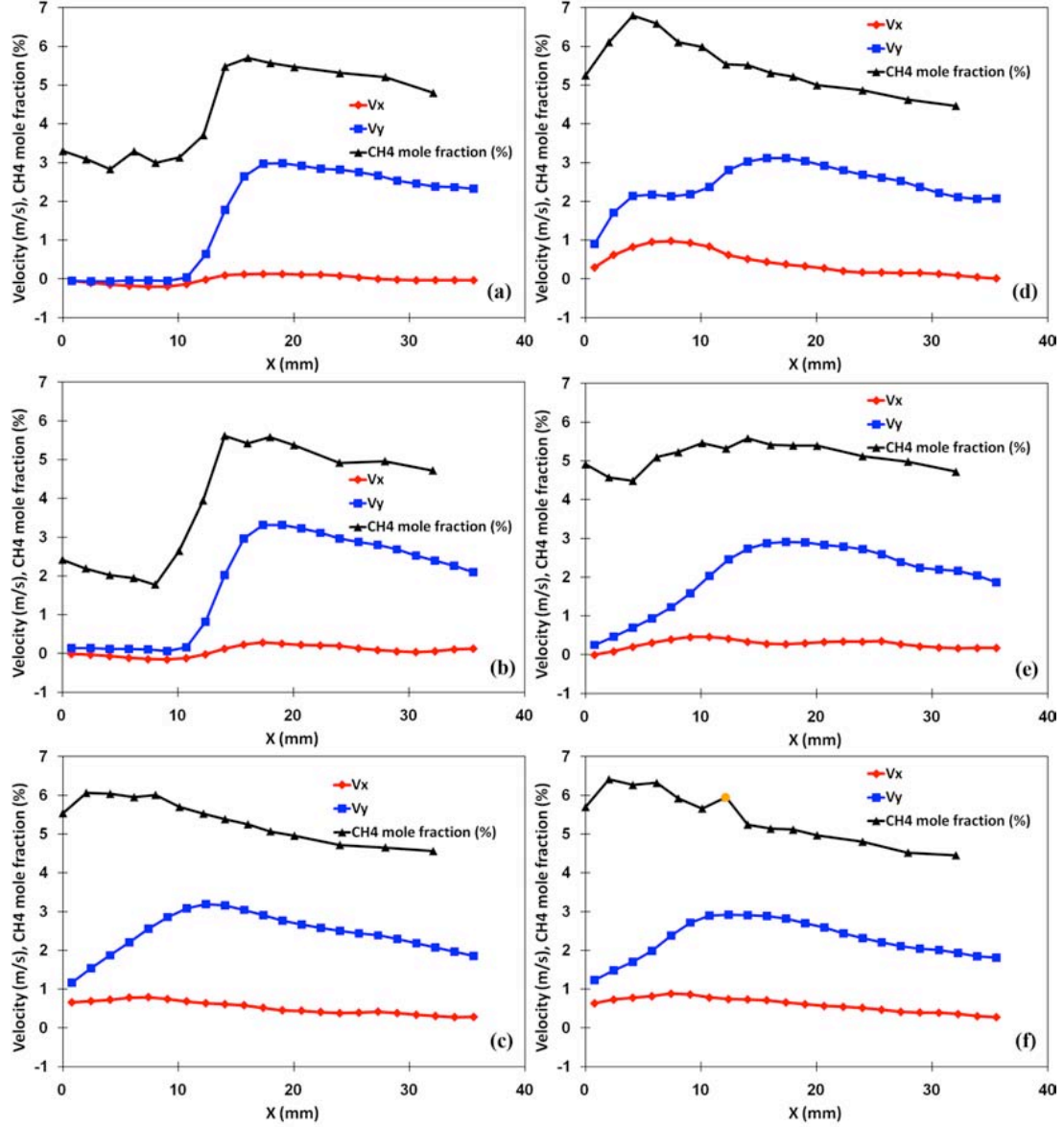


Figure 22: Methane mole fractions and velocity components ( $V_x$  and  $V_y$ ) along the  $x$  direction for six geometries: (a) R, (b) D, (c) T, (d) R+S, (e) D+S and (f) T+S. Experimental conditions were identical to those in Fig. 20. Measurement locations were at  $y = 6.5$  and  $z = 0$ .

### 2.3.5 Flow Fields Near the Base in a Room Temperature Freestream (2D PIV Measurement)

Figure 21 shows instantaneous (Fig. 21a) and ensemble averaged (Fig. 21b) PIV images for the six non-cavity and cavity geometries, i.e., R, D and T, R+S, D+S, and T+S. Also shown in red are pseudo-streamlines. For all the cases shown in Figure 21, the flame was present and the configuration corresponded to the hybrid mode. The flow rate of additional air injection and the resulting nominal flow speed (measured at 2 cm distance away from methane nozzle) were kept identical as 100 SPLM and  $\approx 3$  m/s, respectively. The equivalence ratio of the fully premixed stream also was kept fixed at 0.72 for all images.

As shown in the instantaneous images (especially for R, D, R+S, and D+S geometries), recirculating flow structures, which were believed to play a key role in the bluff body flame stabilization, could be found for all four geometries. For example, one could see clearly strong recirculating pairs with their centers located at  $y \approx 10$  mm and  $y \approx 6$  mm in the R geometry and at  $y \approx 10$  mm and  $y \approx 20$  mm in the D geometry. For the R+S and D+S geometries the structure resided at the height of  $y \approx 5$  mm (R+S) and  $y \approx 2$  mm (D+S). The recirculating pattern was more clear, and its strength was more intense in the non-cavity geometries than in the cavity cases. The recirculation in the cavity cases was less visible because either intense recirculation zones of the local cavity geometries resided in a region where the laser light could not illuminate, e.g., inside of the cavity, or the geometries tended to generate small, multiple vortices rather than one large vortex pair (see Fig. 23 for a more detailed discussion on the characteristics of vortices generated by each geometry).

The vortices generated from the local cavity geometries were more incoherent, i.e., the shedding frequency, size, and locations were more diverse, as described in the liftoff study. Evidence of the incoherent vortices also could be seen in the present study as shown in the averaged PIV images of Fig. 21b. The recirculation pattern for non-cavity geometries was still clear from this figure (especially for R and D geometries); however, no apparent vortex was observed in the cavity geometries (R+S and D+S). This fact implied that the vortices observed in the instantaneous images of the cavity geometries were more random (incoherent) and therefore tended to disappear in the ensemble-averaged images.

Unlike the four geometries D, R, D+S, and R+S, the T and T+S geometries had more direct (i.e., non-recirculating) flow patterns along the slanted side surfaces in the region of interest for which laser illumination was present. The flow pattern was inconsistent with our previous observations (liftoff study), which showed two large, nearly symmetric recirculation zones along the side surfaces for the  $\approx 5.7$  m/s vitiated flow in the absence of additional air injection. Slight misalignment between the direction of fully premixed flow and the air injection in the current configuration induced a small skew of the local flow to the right in the region of interest. The skewed flow, as clearly seen in the averaged field, seemed to eliminate the recirculation zone on the left face in the region of interest and created bent flow along the vortices at  $y \approx 0$  (clockwise direction). There was evidence of a recirculation zone on the right face of the T and T+S bases



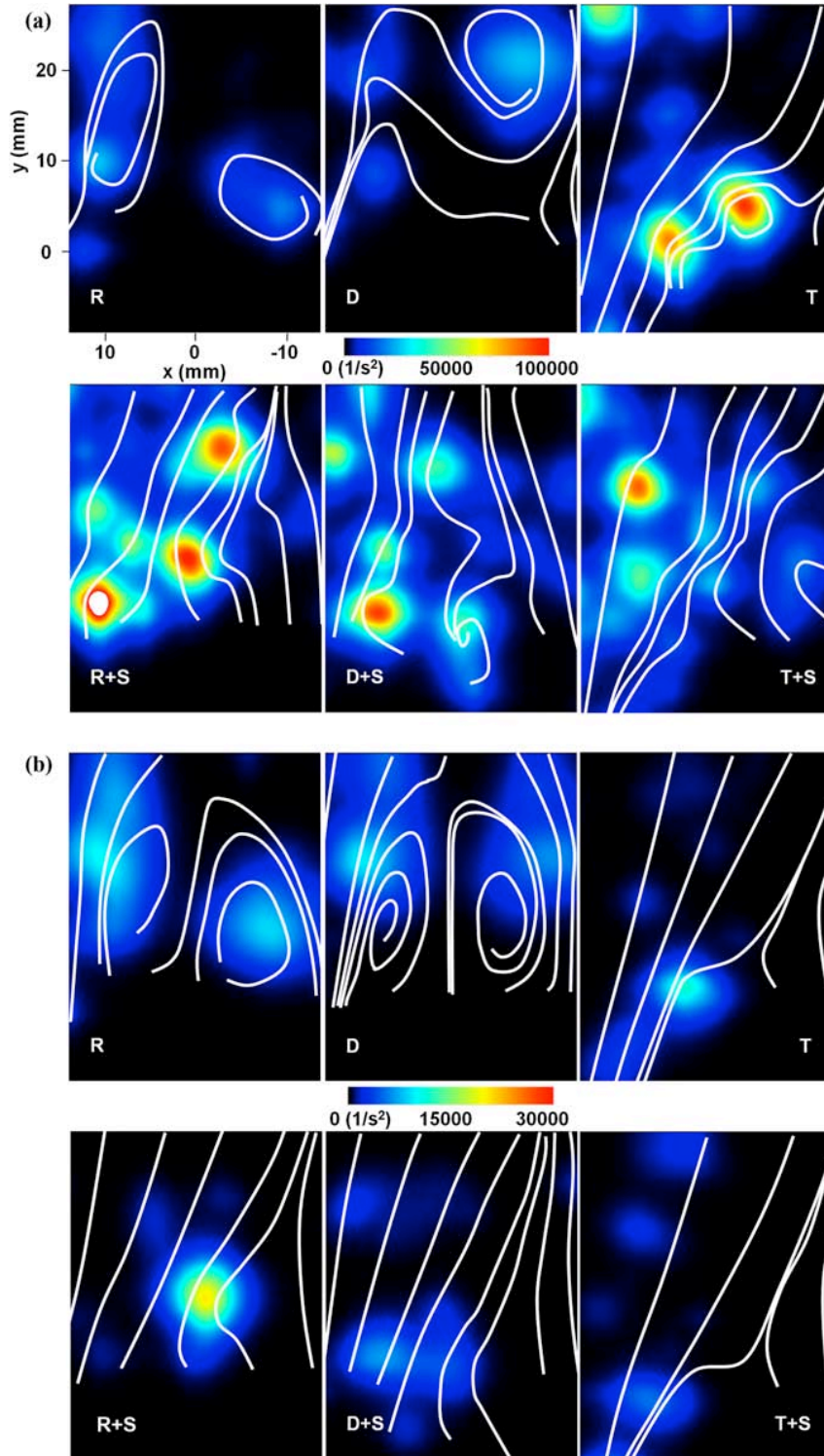


Figure 23: Swirling strength of (a) instantaneous and (b) ensemble averaged velocity fields of the R, D, T, R+S, D+S, and T+S geometries obtained under experimental conditions identical to Fig. 21. The white lines are pseudo streamlines.

(e.g., near  $x = y = -5$ ) from the relatively upright averaged flow field at  $x \approx -5$  –  $-10$ ,  $y = 0$  in Fig. 21b, and the corresponding instantaneous images in Fig. 21a. This small asymmetry might be amplified in geometries such as T and T+S (which showed a higher sensitivity to the flow symmetry because of their sharp vortices) and thus altered the flow pattern of those geometries, resulting in either two or just a single recirculation bubble. This aspect did not seem to change our key results in the current study (i.e., improvement of the blowout limit in the cavity geometries due to geometry’s ability to distribute the fuel in a less diluted manner) in that our observations still held for geometries such as the R and R+S and the D and D+S, which were more robust to the flow asymmetry.

### 2.3.6 Swirling Strengths and Strain Rates Near the Base in a Room Temperature Freestream

Figure 23a shows instantaneous images of swirling strength field (and pseudo streamlines represented by white lines) for the six geometries R, D, T, R+S, D+S, and T+S at experimental conditions identical to those of Fig. 21. It was known that the swirling strength, a measure of how fast the fluid is rotating locally, was a good marker of vortical structures (see Christensen & Wu, 2005). There were more vortices in the bluff body downstream of the cavity geometry (and T geometry) than in non-cavity geometries (especially in the R, R+S, D, and D+S). We believed that more complex back-steps in the geometry helped generate multiple and incoherent vortices.

In Fig. 23b the swirling strength of the averaged velocity field (shown in Fig. 21b) is illustrated, where the swirling strength was defined as the imaginary portion of the complex-conjugate eigenvalues of the local velocity gradient tensor (see Natrajan & Christensen, 2006). Unlike the instantaneous field in Fig. 23a, no noticeable discrepancy existed between the non-cavity and cavity geometries, i.e., there existed a similar number of diffuse vortices in all six cases. This observation (multiple, highly concentrated vortices in an instantaneous field and a smaller number of diffuse vortices in an averaged field shown in the cavity geometries) confirmed that the local cavity geometry could generate incoherent vortices unlike the non-cavity geometries (especially in the R and D geometries).

Finally, the strain rates of the averaged velocity field in the six representative geometries are illustrated in Fig. 24. The experimental conditions were identical to those of Fig. 23. As shown in this figure, the regions of high strain rates were generally large in the non-cavity geometry cases (e.g., the strain rate on the top surface of the R and D geometries), whereas that region was small in cavity geometry (R+S and D+S). We did not believe that this level of strain rate ( $< \approx 100/\text{s}$ ) could cause local extinction, but we expected that the high strain rate in the vicinity of the bluff body seen in the non-cavity geometries did not increase the flame stability. Similar to previous observations, no noticeable difference was found between the T and T+S geometries.

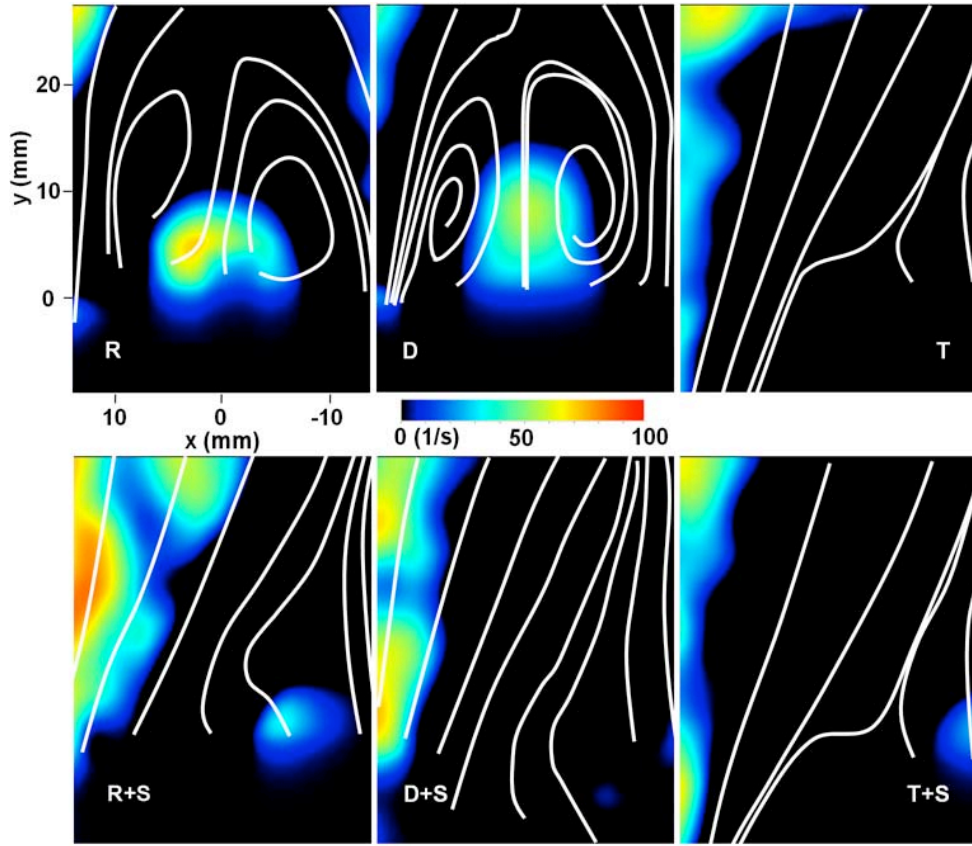


Figure 24: Strain rate obtained from ensemble averaged velocity field. Experimental conditions were identical to that of Fig. 21. The white lines represent the pseudo streamlines.



### 3 Numerical Modeling Using Large-Eddy Simulation

In the previous section, several new flame holder designs were presented with improved stability characteristics. The experimental characterization of the developed geometries was done in a low-speed vitiated flow configuration. In the present section, two different approaches were presented to assist in the development of new flame-holding technologies. The first was a new formulation of Damköhler (Da) number similarity. This technique allowed for a proper definition of Da, such that similarity conditions could be defined for the assessment of flame stabilization. With this method, low-speed experiments could be used to assess afterburner static stability under typical operating conditions. The second was an assessment of the combustion modeling techniques to predict the static stability of the flame-holder configurations presented in Section 2.

#### 3.1 Damköhler Number Similarity for Static Flame Stability in Augmentor Flows

##### 3.1.1 Introduction

Flame holders provided several features important for flame stability. As the presence of the flame holder modified the velocity field, a recirculation zone (RZ) was generated after the flame-holder base. This recirculation zone provided sufficient residence time and chemical heat release needed to ignite the fresh gas mixture. In addition, the shear layer generated around the RZ provided a turbulent mechanism to mix fresh fuel and air with the combustion products from the recirculation zone (Zukowski & Marble (1955); Longwell *et al.* (1953)). Finally, as the flame was stabilized past the flame holder base, combustion products at the end of the recirculation zone were entrained into the RZ to provide a self-ignition mechanism.

The inflow mixture to the augmentor usually was at high-speed and high-temperature. The typical inflow temperatures and velocities for augmentors ranged between 700 and 1000 K and 100 and 200 m/s, respectively (King & Nakanishi (1957)). Under these conditions the experimental assessment of such configurations was complex and expensive. The current work investigated the possibility of utilizing mathematical similarity to test such configurations. Here, we assessed the Damköhler number similarity, which implied that, in the high Reynolds number limit, the flow and the flame characteristics in a high-speed/fast-chemistry case should be similar to a low-speed/slow-chemistry case, as long as the Damköhler number and all the momentum ratios were the same.

Several papers have quantified flame blow-off, and the Damköhler number often was used in the parameterization (Mellor (1980); Radhakrishnan *et al.* (1981)). A comprehensive review of the subject and a collection of data for bluff-body-stabilized flames in augmentor-like systems recently was provided by Shanbhogue *et al.* (2009a). An early attempt to formulate a general theory of premixed flame stabilization behind a bluff body was made by Longwell *et al.* (1953), who derived flame stability curves for different activation energies assuming a second-order

homogeneous reaction at steady-state conditions. King & Nakanishi (1957) investigated the effect of the flame holder geometry on combustion efficiency. They reported a strong correlation between fuel to air ratio at extinction and the inflow parameters of pressure, temperature, and velocity. More recently, two experimental and numerical studies (Kiel *et al.* (2007, 2006)) discussed flame extinction behind a set of bluff-body-stabilized flames. They speculated that three different effects controlled wake-stabilized flames. These effects were viscous forces, inertial forces, and the baroclinic torque generated by the density variation due to combustion. The competition among these effects changed the flame blow-out and extinction characteristics. For high Reynolds numbers, in the square, V-gutter, and circular cylinder flame holders, the latter two effects were found to be most important. At low Reynolds numbers, the viscous forces were found to be more dominant.

The near-blow-off dynamics of a bluff-body-stabilized flame were studied by Lieuwen *et al.* (2007) and Suraj & Lieuwen (2007). The unsteadiness was found to be a major factor that promotes blow-off. Lieuwen and Suraj concluded that the flame blowout could not be explained based on purely steady state characteristics such as the residence and the chemical time scales. They argued that two factors mainly drove flame extinction, the presence of vortex shedding in the wake of the bluff-body and the locally induced strain. The combined effects of these two unsteady factors controlled the path of the reactants and the hot gases, and, under certain conditions, if the recirculation was strong enough, the cold gases could sweep the stabilization point, leading to flame blow-off. In that sense, the onset of the large-scale deterministic unsteadiness could be seen as a precursor for blow-off; therefore, in this report, although the main interest was in actual blow-off, we only considered the near-blow-off regime, which was characterized by vortex shedding. We then used the characteristics of that large-scale unsteadiness as a surrogate in the discussion of static flame stability without determining the actual stability limits.

Several computational studies of bluff-body flame stabilization have been reported. Porumbel & Menon (2006), for instance, performed an LES study of a bluff-body-stabilized premixed flame. They concluded that the baroclinic torque generated by combustion weakened the Kelvin-Helmholtz instability and suppressed the von Kármán vortex street observed in the non-reactive flow simulation. The same conclusion was supported by Mehta & Soteriou (2003) and Ghoniem & Krishnan (1988). Khosla *et al.* (2007) studied a bluff-body configuration similar to the current work. They highlighted the effect of suppressing the von Kármán shedding on the flame blowout characteristics. By using a tabbed bluff-body, the coherence of the vortex shedding between the upper and the lower surface of the bluff-body was disrupted, such that the asymmetrical vortex shedding mode could be eliminated. Knaus *et al.* (2008) and Roach *et al.* (2008) used different numerical approaches in FLUENT ([www.ansys.com](http://www.ansys.com)) to predict the Damköhler number in a V-gutter-stabilized flame. They defined the local chemical time scale based on the extinction strain rate using a single-step global chemistry. This extinction strain rate was found to increase with the global equivalence ratio.

All these experimental and computational studies have contributed to the understanding of

bluff-body supported flame stabilization; however, there still is a need for fundamental studies and flame holder testing. Experimental investigations can be simplified greatly by considering Damköhler similarity. The basic idea is that all flow and combustion characteristics, including stability, should be similar for different operating conditions, as long as all non-dimensional groups describing the problem are the same. One of the more important non-dimensional groups important for combustion problems is the Damköhler number, which is defined as the ratio of characteristic flow and chemistry time scales; however, changing the operating conditions while keeping the Damköhler number constant is not trivial. In this report, a method for ensuring Damköhler number similarity was provided and validated.

Numerical simulations for three different conditions were performed using large-eddy simulations, where combustion was modeled using the flamelet progress variable (FPV) approach (Pierce & Moin, 2004). The configuration was for a bluff-body-stabilized flame in a vitiated flow. Methane fuel was injected in the cross-stream direction from the bluff-body surface. Simulation results for a reference case were compared with experimental data, which also were presented in this report. The inflow temperature and chemical composition were varied to change the mutual effect between mixing and chemical time scales, and hence the Damköhler number. The inflow chemical variation and the Damköhler number were found to affect both the flame stabilization and the lift-off characteristics. The stagnation point position in the wake of the bluff-body and the lift-off height were monitored for all three test cases to assess the Damköhler number similarity.

### 3.1.2 Numerical Formulation

**Filtered Flow Equations** - All simulations reported here were performed using the Stanford high-order finite difference NGA solver (Desjardins *et al.* (2008)). The numerical schemes used for the spatial discretization were described in Desjardins *et al.* (2008) and were based on the work of Morinishi *et al.* (1998). The describing equations were in the low Mach number formulation. The scheme was staggered in space and time (Pierce & Moin (2001)). The staggering allowed for secondary conservation, which guaranteed the suppression of numerically caused instability. Hence, no artificial damping was required, which allowed for high accuracy large-eddy simulations. In this project, second-order time and space discretization were used. A semi-implicit iterative technique, described below, was employed to integrate the system of equations using the fractional step method. More details about the numerical methods can be found elsewhere (Pierce & Moin (2001), Desjardins *et al.* (2008)).

By applying a spatial filter, denoted here by an overline, to the Navier Stokes equations and using the Favre decomposition, defined for a general variable  $\phi$  as  $\tilde{\phi} = \frac{\overline{\rho\phi}}{\bar{\rho}}$ , the continuity and the momentum equations can be written as:

$$\begin{aligned}\frac{\partial \bar{\rho}}{\partial t} + \frac{\partial \bar{\rho} \tilde{u}_j}{\partial x_j} &= 0, \\ \frac{\partial \bar{\rho} \tilde{u}_i}{\partial t} + \frac{\partial \bar{\rho} \tilde{u}_i \tilde{u}_j}{\partial x_j} &= -\frac{\partial \bar{p}}{\partial x_i} + \frac{\partial \tilde{\sigma}_{ij}}{\partial x_j} - \frac{\partial \tau_{ij}}{\partial x_j}.\end{aligned}\quad (1)$$

Here,  $\rho$  is the density,  $u_i$  is the velocity,  $p$  is the pressure,  $t$  is the time,  $x_i$  are the spatial coordinates, and the filtered shear stress is written as

$$\tilde{\sigma}_{ij} = 2\mu \left( \tilde{S}_{ij} - \frac{1}{3} \tilde{S}_{kk} \delta_{ij} \right), \quad (2)$$

where  $\tilde{S}_{ij} = \frac{1}{2} \left( \frac{\partial \tilde{u}_i}{\partial x_j} + \frac{\partial \tilde{u}_j}{\partial x_i} \right)$  is the strain rate tensor and  $\delta_{ij}$  is the Kronecker symbol. The summation over repeated indices is implied, and  $\mu$  is the dynamic viscosity. In the above equations, the effect of the subgrid scales on the resolved scales is represented by the sub-filter stresses  $\tau_{ij} = \bar{\rho} (\widetilde{u_i u_j} - \tilde{u}_i \tilde{u}_j)$ . The sub-filter stresses are modeled using an eddy viscosity assumption (Moin *et al.* (1991)) as

$$\tau_{ij} - \frac{1}{3} \tau_{kk} \delta_{ij} = -2\mu_t \left( \tilde{S}_{ij} - \frac{1}{3} \tilde{S}_{kk} \delta_{ij} \right), \quad (3)$$

The sub-filter eddy viscosity  $\mu_t$  and  $\tau_{kk}$  are modeled as

$$\begin{aligned}\mu_t &= C_\mu \bar{\rho} \Delta^2 |\tilde{S}|, \\ \tau_{kk} &= 2C_K \bar{\rho} \Delta^2 |\tilde{S}|^2.\end{aligned}\quad (4)$$

In these equations  $\Delta$  is the filter width,  $|\tilde{S}| = \sqrt{2\tilde{S}_{ij}\tilde{S}_{ij}}$ , and  $C_\mu$  and  $C_K$  are computed dynamically based on the approach of Moin *et al.* (1991). The density  $\bar{\rho}$  is calculated from the combustion model described in the next section.

**Flamelet Progress Variable Approach** - The flamelet/progress variable (FPV) approach developed by Pierce & Moin (2004) is based on the flamelet concept (Peters (1984)). This approach assumes that the chemical time scales are short enough that chemical reactions occur in thin layers around stoichiometric conditions (Pitsch (2006)). The flamelet approach relates the species mass fractions and the energy to the mixture fraction through the flamelet equations, which are given as

$$\rho \frac{\partial \Psi}{\partial t} - \rho \frac{\chi}{2} \frac{\partial^2 \Psi}{\partial Z^2} = \dot{\omega}, \quad (5)$$

where  $Z$  is the mixture fraction,  $\Psi = (T, y_i)^T$  is a vector that contains the species mass fractions  $y_i$  and the temperature  $T$ .  $\dot{\omega}$  is the vector of chemical source terms for the scalars  $\Psi$ , and  $\chi$  is the scalar dissipation rate.

In the FPV model, solutions of Eq. 5 are tabulated and parameterized by the mixture fraction and a reactive scalar  $\lambda$ . As a result, a tabulated form  $\Phi$  of the solutions of Eq. 5 can be written

as  $\Phi = \mathcal{F}_\Phi(Z, \lambda)$ . The parameter  $\lambda$  is defined through the progress variable  $C$ , which is defined here as the sum of the mass fractions of  $\text{CO}_2$ ,  $\text{CO}$ ,  $\text{H}_2\text{O}$ , and  $\text{H}_2$ . The definition of  $\lambda$  is discussed in more detail in Ihme *et al.* (2005), but the most important feature is that it is defined to be independent of mixture fraction. The mean quantities then can be computed from

$$\tilde{\Phi}(x_i, t) = \int_0^1 \int_0^\infty \Phi(Z, \lambda) \tilde{P}(Z, \lambda; x_i, t) dZ d\lambda, \quad (6)$$

where  $\tilde{P}(Z, \lambda; x_i, t)$  is the joint probability density function (pdf) of  $Z$  and  $\lambda$ . Since  $\lambda$  and  $Z$  are defined to be independent, their joint PDF can be obtained from the product of the marginal PDFs.

The mixture fraction marginal PDF  $\tilde{P}(Z)$  is assumed to be a beta distribution (Pierce & Moin (2004)) and the reactive scalar PDF a delta function at its mean. These assumptions lead to a representation of the flamelet library ( $\mathcal{F}$ ) as

$$\tilde{\Phi} = \mathcal{F}_\Phi^\lambda(\tilde{Z}, \widetilde{Z''^2}, \tilde{\lambda}). \quad (7)$$

Writing Eq. 7 for the progress variable as

$$\tilde{C} = \mathcal{F}_C^\lambda(\tilde{Z}, \widetilde{Z''^2}, \tilde{\lambda}), \quad (8)$$

the reaction progress parameter  $\lambda$  can be replaced by the progress variable. Hence, using Eqs. 7 and 8, the flamelet library can be written as

$$\tilde{\Phi} = \mathcal{F}_\Phi^C(\tilde{Z}, \widetilde{Z''^2}, \tilde{C}). \quad (9)$$

Then, three parameters have to be computed, namely the filtered mixture fraction  $\tilde{Z}$ , the sub-filter scalar variance  $\widetilde{Z''^2}$ , and the filtered progress variable  $\tilde{C}$ . Here the scalar variance  $\widetilde{Z''^2}$  is evaluated using an algebraic model (Pierce & Moin (1998)). The model assumes homogeneity and local equilibrium for the sub-grid scales and is given as

$$\widetilde{\bar{\rho} Z''^2} = C_Z \Delta^2 \bar{\rho} |\nabla \tilde{Z}|^2, \quad (10)$$

where the mixture fraction coefficient  $C_Z$  is computed dynamically. The second parameter is the filtered mixture fraction  $\tilde{Z}$ , for which a transport equation is solved

$$\frac{\partial \bar{\rho} \tilde{Z}}{\partial t} + \nabla \cdot (\bar{\rho} \tilde{u} \tilde{Z}) = \nabla \cdot (\bar{\rho} (D_Z + D_T) \nabla \tilde{Z}). \quad (11)$$

The mixture fraction diffusivity  $D_Z$  is obtained from Eq. (6), and  $D_T$  is the turbulent eddy diffusivity given by Pierce & Moin (1998)

$$D_T = C_T \Delta^2 |\tilde{S}|, \quad (12)$$

where  $C_T$  is computed in a dynamic procedure (Moin *et al.* (1991)). Finally, the filtered progress variable is obtained by solving the transport equation of  $\tilde{C}$  as:

$$\frac{\partial \bar{\rho} \tilde{C}}{\partial t} + \nabla \cdot (\bar{\rho} u \tilde{C}) = \nabla \cdot (\bar{\rho} (D_C + D_T) \nabla \tilde{C}) + W_C, \quad (13)$$

where  $D_C$  is the progress variable diffusivity,  $W_C = \bar{\rho} \left( \frac{\dot{m}_C}{\rho} \right)$  is the Favre-averaged net mass production rate of  $C$ , and  $\dot{m}_C$  is the net production rate in (kg/m<sup>3</sup>s).

The flamelet/progress variable model has been validated in several *a priori* and *a posteriori* studies, including applications to predict NO<sub>x</sub> (Ihme & Pitsch (2008a)) and local extinction and reignition (Ihme *et al.* (2005); Ihme & Pitsch (2008b,c)). Next we reformulate the modeled governing equations in the non-dimensional form to derive similarity conditions and the role of the Damköhler number.

**Non-Dimensional Governing Equations** - In the following, we considered a flame stabilized on a bluff-body flame holder. The oxidizer stream was vitiated, and the fuel was injected through the flame holder in cross-flow. To derive the non-dimensional governing equations, the following relations were defined, where the subscript ( $\infty$ ) referred to the reference values at the vitiated inflow conditions and the superscript ( $*$ ) referred to the non-dimensional values:

$$\begin{aligned} \tilde{u}_i^* &= \frac{\tilde{u}_i}{U_\infty}, & x_i^* &= \frac{x_i}{D_b}, & \bar{\mu}^* &= \frac{\bar{\mu}}{\mu_\infty}, \\ \mu_T^* &= \frac{\mu}{\rho_\infty U_\infty D_b}, & t^* &= \frac{t U_\infty}{D_b}, & \tilde{C}^* &= \frac{\tilde{C}}{C_{\text{ref}}}, \\ \bar{\rho}^* &= \frac{\bar{\rho}}{\rho_\infty}, & \bar{p}^* &= \frac{\bar{p}}{\rho_\infty U_\infty^2}, & D_C^* &= \frac{D_C}{D_{Z,\infty}}, \\ D_Z^* &= \frac{D_Z}{D_{Z,\infty}}, & D_T^* &= \frac{D_T}{U_\infty D_b}, & \chi^* &= \frac{\chi}{\chi_q}. \end{aligned} \quad (14)$$

The reference length scale was chosen to be a characteristic length of the flame holder  $D_b$ . The scalar dissipation rate  $\chi$  was non-dimensionalized by its value at the quenching conditions  $\chi_q$ . The mixture fraction as a normalized quantity needed no further normalization. The progress variable mass fraction in the vitiated coflow was chosen as a reference value for the reaction progress variable,  $C_{\text{ref}} = C_\infty$ . Another reasonable choice was to use the progress variable value at complete conversion of fuel and oxidizer to reaction products. That definition could be used if the more general case of non-vitiated flow was considered.

By substitution of Eqs. (14) into the modeled form of Eqs. (1), the following non-dimensional form was obtained:

$$\begin{aligned} \frac{\partial \bar{\rho}^*}{\partial t^*} + \frac{\partial \bar{\rho}^* \tilde{u}_j^*}{\partial x_j^*} &= 0, \\ \frac{\partial \bar{\rho}^* \tilde{u}_i^*}{\partial t^*} + \frac{\partial \bar{\rho}^* \tilde{u}_j^* \tilde{u}_i^*}{\partial x_j^*} &= -\frac{\partial \bar{p}^*}{\partial x_i^*} + \frac{1}{\text{Re}_\infty} \frac{\partial \tilde{\sigma}_{ij}^*}{\partial x_j^*} - \frac{\partial \tau_{ij}^*}{\partial x_j^*}. \end{aligned} \quad (15)$$

Here, the Reynolds number of the vitiated inflow was given by  $\text{Re}_\infty = \frac{\rho_\infty U_\infty D_b}{\mu_\infty}$ . Following the same procedure with Eqs. (11) and (13), the filtered progress variable and the filtered mixture

fraction equations in the non-dimensional form became

$$\frac{\partial \bar{\rho}^* \tilde{Z}}{\partial t^*} + \frac{\partial}{\partial x_i^*} \left( \bar{\rho}^* \tilde{u}_i^* \tilde{Z} \right) = \frac{1}{\text{Re}_\infty \text{Sc}_\infty} \frac{\partial}{\partial x_i^*} \left( \bar{\rho}^* D_Z^* \frac{\partial \tilde{Z}}{\partial x_i^*} \right) + \frac{\partial}{\partial x_i^*} \left( \bar{\rho}^* D_T^* \frac{\partial \tilde{Z}}{\partial x_i^*} \right), \quad (16)$$

$$\frac{\partial \bar{\rho}^* \tilde{C}^*}{\partial t^*} + \frac{\partial}{\partial x_i^*} \left( \bar{\rho}^* \tilde{u}_i^* \tilde{C}^* \right) = \frac{1}{\text{Re}_\infty \text{Sc}_\infty} \frac{\partial}{\partial x_i^*} \left( \bar{\rho}^* D_C^* \frac{\partial \tilde{C}^*}{\partial x_i^*} \right) + \frac{\partial}{\partial x_i^*} \left( \bar{\rho}^* D_T^* \frac{\partial \tilde{C}^*}{\partial x_i^*} \right) + \frac{W_C D_b}{\rho_\infty C_{\text{ref}} U_\infty}, \quad (17)$$

where  $\text{Sc}_\infty = \frac{\mu_\infty}{\rho_\infty D_{Z,\infty}}$  was the Schmidt number of the vitiated inflow. Further treatment for the progress variable source term will be discussed in the next subsection. Finally, the state relationship for the thermodynamic and chemical variables was computed from the non-dimensional equation of state:

$$\Phi^* = \mathcal{F}_\Phi \left( \tilde{Z}, \tilde{C}^* \right). \quad (18)$$

Irrespective of the specific values of the parameters appearing in the problem, Eqs. (15)-(18) would have the same solution if all non-dimensional groups appearing in the non-dimensional equations had the same value and if the non-dimensional boundary conditions were the same. The inflow boundary conditions for the cross flow and the jet were uniform with bulk velocities  $U_\infty$  and  $U_J$ , respectively, where subscript  $J$  stood for conditions in the fuel jets; therefore, the inflow boundary conditions for the vitiated cross flow in the non-dimensional form were:

$$\begin{aligned} \langle u_{1,\infty}^* \rangle &= 1.0 \\ \langle u_{2,\infty}^* \rangle &= 0.0 \\ \langle u_{3,\infty}^* \rangle &= 0.0 \\ C_\infty^* &= 1.0 \\ Z &= 0.0. \end{aligned} \quad (19)$$

Similarly, the non-dimensional jet inflow conditions were:

$$\begin{aligned} \langle u_{1,j}^* \rangle &= 0.0 \\ \langle u_{2,j}^* \rangle &= 0.0 \\ \langle u_{3,j}^* \rangle &= \frac{r}{\sqrt{2\rho_j^*}} \\ C_j^* &= 0.0 \\ Z &= 1.0. \end{aligned} \quad (20)$$

where  $r = \sqrt{\frac{2\rho_J U_J^2}{\rho_\infty U_\infty^2}}$  was the momentum ratio. The above equations showed that the non-dimensional solution  $\bar{\rho}^*, \tilde{u}_i^*, \bar{p}^*, \tilde{Z}, \tilde{C}^*$  at  $t^*, x_i^*$  was described by the non-dimensional groups  $\text{Re}_\infty, \text{Sc}_\infty, r$ , and one more that came from the chemical source term in Eq. 17. Assuming that

the Reynolds number was large, that molecular Schmidt number effects were unimportant, and keeping  $r$  fixed, the only free parameter was the Damköhler number<sup>1</sup>, which was discussed in the following section.

**Damköhler Number Similarity** - The characteristic Damköhler number was defined as the ratio of the characteristic flow or mixing time scale to the characteristic chemical time scale

$$\text{Da} = \frac{\tau_{\text{flow,ref}}}{\tau_{\text{chem,ref}}}, \quad (21)$$

where the flow time scale was defined as  $\tau_{\text{flow}} = \frac{D_b}{U_\infty}$ , here based on the bluff-body width  $D_b$  and the cross flow velocity  $U_\infty$ . The chemical time scale could be defined in many different ways. For single step chemistry, it typically was defined as the chemical source term divided by a reactant concentration. In previous work, Pitsch & Fedotov (2001) and Pitsch *et al.* (2003) derived an expression for the non-dimensional source term for single-step chemistry. They showed that the source term and equivalently the chemical time scale were functions of unique non-dimensional quantities that depended on the frequency factor of the one-step mechanism and the chemical and thermal boundary conditions; therefore, mathematical similarity could be achieved for such a case. In the interaction of realistic chemistry with flow and transport processes, different combustion phenomena occurred, such as auto-ignition, premixed flame propagation, and non-premixed combustion. Because different chemical reactions might be important for each of these processes, a unique definition of the relevant chemical time scale associated with a particular reaction was not possible. Each chemical reaction had its own time scale and Damköhler number. As an example, if mathematical similarity was to be achieved at a higher flow velocity, which implied a smaller flow time scale, the chemical time scales needed to be reduced such that the same overall Damköhler number was achieved. Typical ways to change the chemical time scales were changes in the temperature, the equivalence ratio, or dilution. It was obvious that not all chemical time scales could be changed in the same way, because the chemical time scales depended on both temperature through activation energy and species concentrations, the variation was different for each reaction; therefore, only one of many chemical time scales could be adjusted. The choice of this time scale should be related to the physics of the dominating combustion phenomenon. For example, in premixed flames, the flame propagation mechanism was important, while for auto-ignition stabilized flames, initiation reactions might be rate-limiting.

Figure 25 shows the steady solutions of the flamelet equations for varying vitiated air temperatures and stoichiometric scalar dissipation rates. As the vitiated inflow temperature increased, radical-producing reactions were accelerated, and chemical time scales generally decreased, allowing for a higher quenching scalar dissipation rate. The effect on scalar dissipation rate was shown in Figs. 26 and 27. Figure 26 shows the normalized chemical source term of the progress

---

<sup>1</sup>Note that a low Mach number scaling was used for the pressure, which implied that the Mach number was low enough that compressible effects were unimportant. This was the case for the conditions considered here; however, the assumption that the effect of compressibility could be neglected in the assessment of static flame stability in augmentors needed future validation



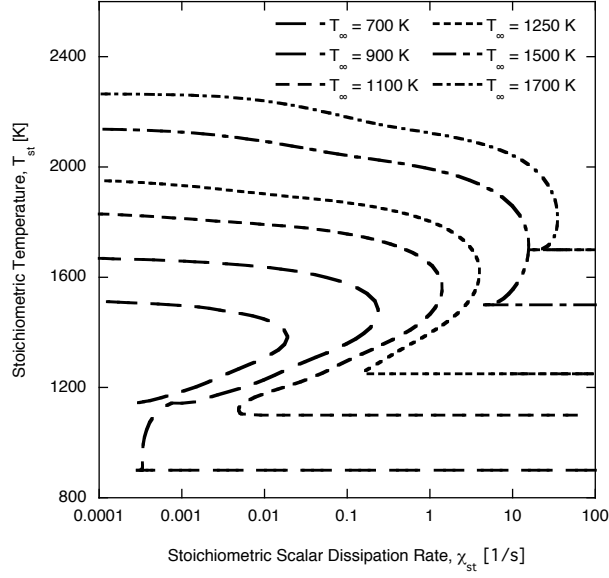


Figure 25: Effect of the vitiated flow temperature ( $T_\infty$ ) on quenching and ignition characteristics

variable as a function of the non-dimensional scalar dissipation rate for the same variation in vitiated inflow temperatures as in Fig. 25. The inverse of a chemical time scale defined as

$$\tau_{\text{chem}} = \frac{\rho_\infty C_{\text{ref}}}{W_{C,\text{st}}} \quad (22)$$

is shown in Fig. 27. As the dissipation rate increased, which corresponded to a decrease in the flow time scale, the chemical source term went up, and the chemical time scale decreased. The reason was that, while the stoichiometric temperature decreased, which lead to an increased chemical time scale, stronger mixing increased the stoichiometric concentrations of the fuel, oxidizer, and related products, which made reactions faster. The resulting effect was a net decrease in the chemical time scale, until the effect of decreasing temperature started to dominate the chemical source terms, which ultimately lead to extinction. The balance between chemistry and transport at extinction was particularly important, since it provided the largest possible chemical source term and the smallest possible chemical time scale. Because the extinction process was important for static stability, the minimum chemical time scale corresponding to the maximum chemical source term should be used here to define the Damköhler number of the reaction progress variable  $\text{Da}_C$ . With

$$\tau_{\text{chem,ref}} = \frac{\rho_\infty C_{\text{ref}}}{W_{C,\text{max}}} , \quad (23)$$

and with

$$W_C^* = \frac{W_C}{W_{C,\text{max}}} \quad (24)$$

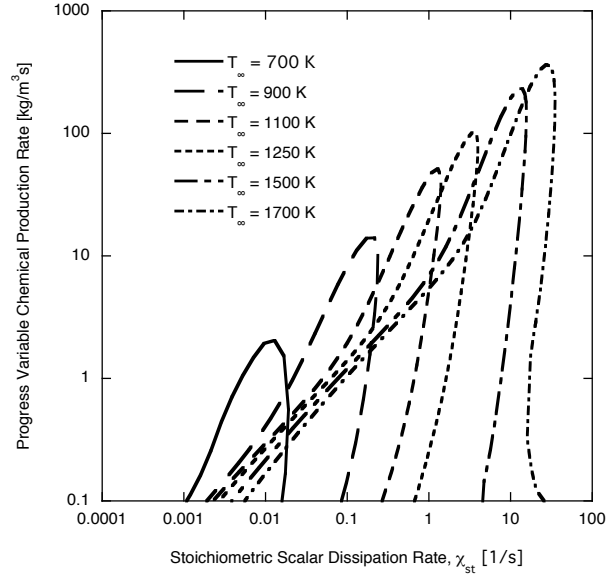
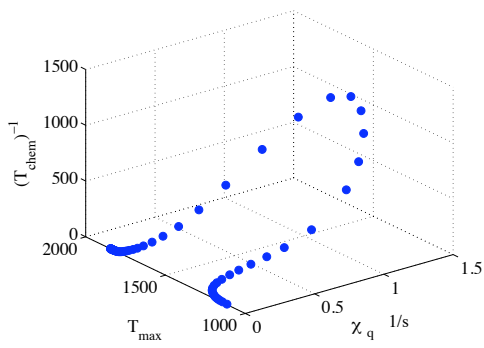
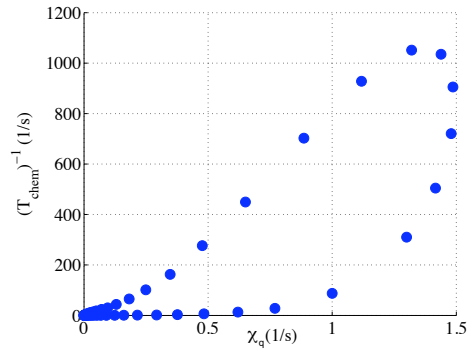


Figure 26: Variation of normalized chemical production rate of progress variable with scalar dissipation rate



(a) 3D view



(b) Projection into  $\chi_{st} - \tau_{chem}^{-1}$  plane

Figure 27: Variation of chemical time scale along S-shaped curve

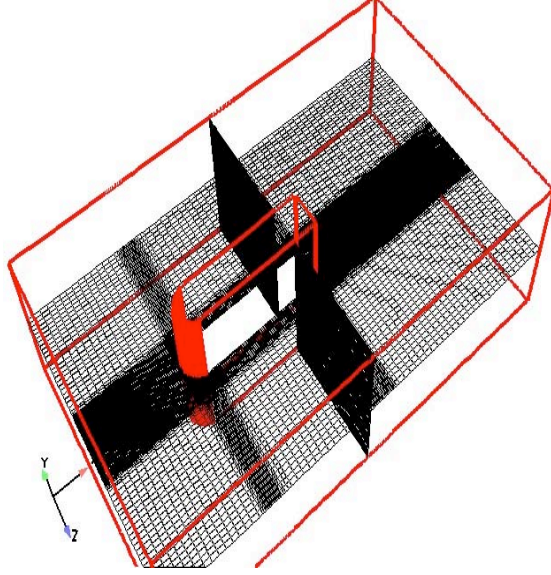


Figure 28: Computational mesh for LES of the flame holder geometry

Eq. (17) can be rewritten as

$$\frac{\partial \bar{\rho} \tilde{C}}{\partial t} + \frac{\partial}{\partial x_i} \left( \bar{\rho} \tilde{u}_i \tilde{C} \right) = \frac{1}{\text{Re}_\infty \text{Sc}_\infty} \frac{\partial}{\partial x_i} \left( \bar{\rho} D_C \frac{\partial \tilde{C}}{\partial x_i} \right) + \frac{\partial}{\partial x_i} \left( \bar{\rho} D_T \frac{\partial \tilde{C}}{\partial x_i} \right) + W_C^* Da_C, \quad (25)$$

where  $Da_C$  was defined according to Eq. (21).

### 3.1.3 Numerical Method

In the numerical simulations, the bluff-body geometry was represented using an immersed boundary (IB) technique, as described by Kang *et al.* (2009). The IB method was based on the reconstruction of the velocity components on the faces of the staggered interface cell by linear interpolation from the adjacent fluid cells solved by the Navier-Stokes solver. These reconstructed velocities then were used as boundary condition for the solver around the IB.

The bluff-body geometry and the grid are shown in Fig. 28. The computational grid consisted of  $110 \times 40 \times 76$  mesh points in the flow direction, in the lateral direction, and across the bluff body. The domain was assumed periodic in the lateral direction, and the mesh was refined in the regions around the bluff-body. Methane jets at 300 K were injected from two circular ports located 0.5 inch upstream the base of the bluff-body. A flow of vitiated hot mixture was injected in the stream-wise direction at an equivalence ratio of  $\Phi_\infty = 0.67$ . The jet and the vitiated mixture mass flow rates were varied to change the effective flow time scales, while keeping the momentum ratio the same.

To assess and validate the proposed method to achieve Damköhler number similarity, three different test cases were chosen. The flow conditions for the three test cases were summarized in Table 1.

	$U_\infty$	$U_j$	$T_\infty(K)$	$\nu_\infty$	$\tau_{\text{flow,ref}}$	$\tau_{\text{chem,ref}}$	$\text{Da}_C$	$\text{Re}_\infty$	$\text{Sc}_\infty$	$\text{St}_{\text{RZ}}$
Case 1	3.6	2.23	1100	$1.4 \cdot 10^{-4}$	0.0071	0.0011	6.429	653	0.16	0.20
Case 2	7.8	4.43	1300	$1.8 \cdot 10^{-4}$	0.00327	0.00051	6.429	1101	0.16	0.18
Case 3	22.7	9.75	1700	$2.6 \cdot 10^{-4}$	0.00118	1.74E-4	6.429	2218	0.16	0.22

Table 1: Flow test conditions, where  $T_\infty$  was the temperature of the vitiated hot stream [K],  $\nu_\infty$  was the inflow kinematic viscosity [ $\text{m}^2/\text{s}$ ],  $U_\infty$  was the vitiated air bulk velocity [ $\text{m/s}$ ],  $U_j$  was the fuel jet velocity [ $\text{m/s}$ ],  $\tau_{\text{flow}}$  was the characteristic flow time [s],  $\tau_{\text{chem}}$  was the characteristic chemical time [s],  $\text{Da}_C$  was the characteristic Damköhler number,  $\text{Re}_\infty$  and  $\text{Sc}_\infty$  were the vitiated hot flow Reynolds number and Schmidt number, and  $\text{St}_{\text{RZ}} = f_{\text{RZ}}D_\infty/U_\infty$  was the Strouhal number of the oscillation of the recirculation zone, where  $f_{\text{RZ}}$  was the corresponding frequency.

The conditions of the first test case matched the experimental setup, while for the other two cases, the flow and the chemical conditions were varied such that the Damköhler number was the same. The first test case represented low-speed/slow chemistry, while the second and the third case represented high-speed/fast chemistry. The inflow composition was computed as the equilibrium composition of the methane-air mixture at the inflow equivalence ratio and temperature. These values then were used to set the boundary conditions for the flamelet equations.

### 3.1.4 Results

The instantaneous recirculation zone (RZ) and flame structure are shown in Fig. 29. The three flames showed similar flame and RZ structure. The recirculation zone was found to extend over the bluff-body base and was surrounded by the flame surface. The effect of the outer shear layer was shown to wrinkle the flame surface, causing shedding of mixed burned/unburned gases.

Figure 30 shows the mean non-dimensional axial velocity distribution at different heights above the bluff-body base. Downstream of the bluff body, a recirculation zone was established. The RZ extended to a distance of around 50 mm above the base and around 20 mm from the centerline. Experimental data were available at three locations and were compared with the simulation results. The PIV results were ensemble-averaged over 100 frames, with streamwise averaging resulting in a statistical accuracy estimated at 1%. Good agreement was observed between the LES and the experimental data; however, the measured velocity profiles were slightly asymmetric. This asymmetry in the experimental results was due to the fact that the inflow field was not perfectly uniform. The solutions of all three computed cases collapsed onto each other, which confirmed the Damköhler number similarity of the three flames.

A comparison of the normalized mean temperature is shown in Fig. 31. The three test cases exhibited the same flame structure; however, at the first location, the test case 3 flame showed a small deviation at the edge of the shear layer. The mean flame and RZ structure showed a

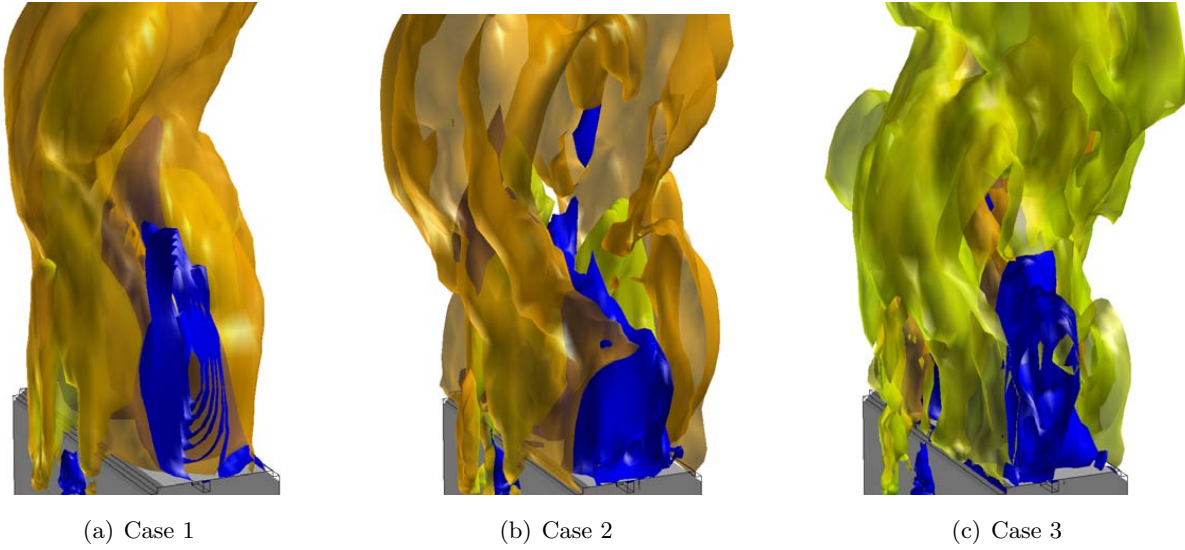


Figure 29: Iso-surfaces of negative axial velocities (blue) combined with temperature iso-surfaces,  $T = 1400$  K for case 1,  $T = 1450$  K and  $1550$  K for case 2, and  $T = 1850$  K and  $1950$  K for case 3, all colored by progress variable.

mathematically similar solution, again underlining the applicability of the proposed Damköhler number similarity for the given conditions of the three studied flames.

As the studied flames showed similar RZ structure, they also showed similar flame stability features. The flame stabilization point was defined as the closest point to the bluff-body where reaction happens. Since this flame was wake stabilized, the wake structure controlled the flame stability characteristics. Furthermore, as long as the chemical time scale was short enough to compete with residence time, the flame would stabilize and would not blow off. The shorter the chemical time scale, the higher the flow speed was needed to stabilize the flame at the same height. To further assess the validity of the current approach, the flame height above the base was measured and compared with experimental data. By analogy with the experiment, the flame height was defined as the first point above the base (at the median plane), where burning stoichiometric conditions were found. The flame height was computed as the average from many snapshots obtained over a long compute time. The averaged computed values were around  $10.5$  mm,  $11.6$  mm, and  $13.2$  mm for the three test cases, respectively, which were comparable to the  $12$  mm reported in the experiment.

Next the flame/wake dynamics were studied to illustrate the similarity in the overall behavior. In the low-speed/slow-chemistry flame, case 1, the RZ tip was found to oscillate at a frequency of  $28$  Hz, which was induced by the vortex shedding. Figure 32 shows eight instantaneous snapshots at the plane  $Y = 10$  mm for case 1 over a complete cycle. The temperature distribution was combined with the contour of zero axial velocity to show the extent of the recirculation zone. The flame boundaries were shown by plotting the contour of the stoichiometric mixture fraction

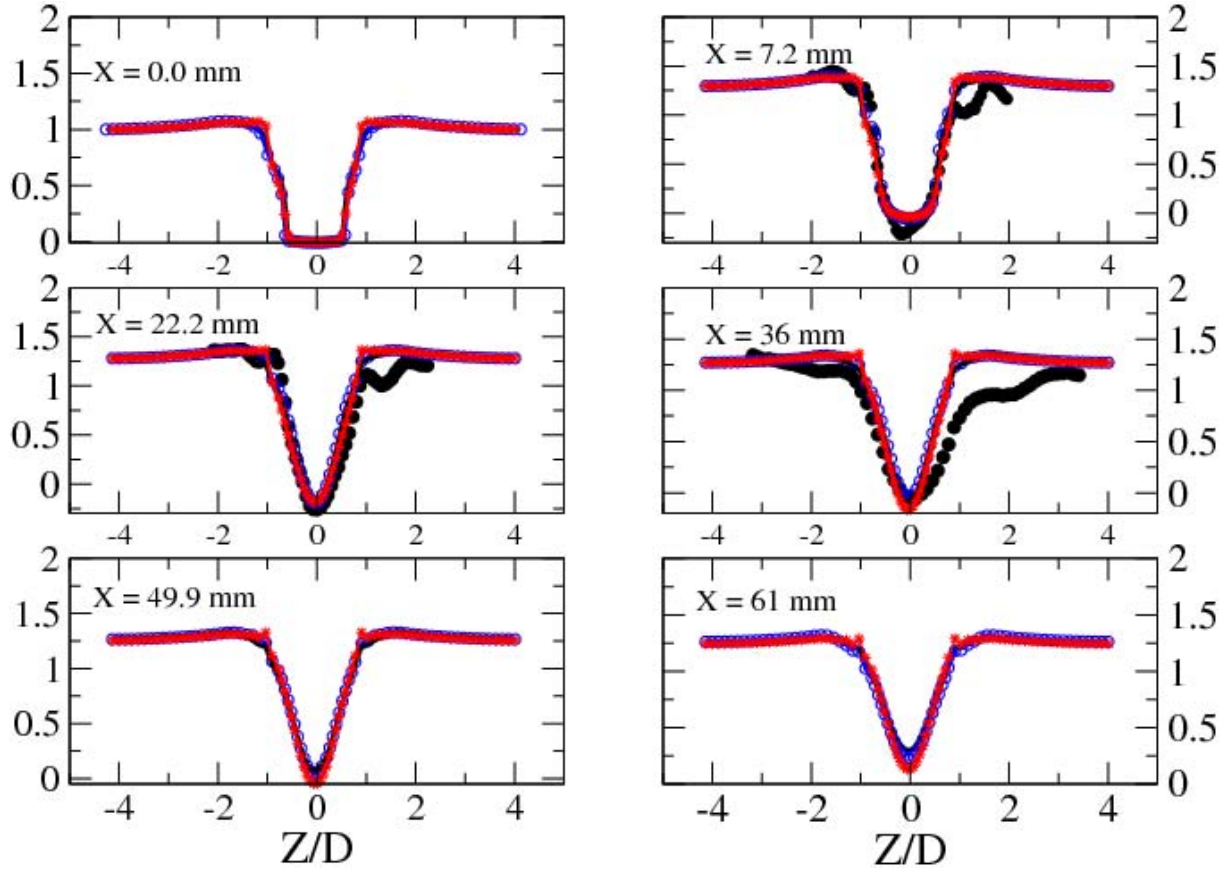


Figure 30: Time-averaged non-dimensional axial velocity  $\langle \tilde{U} \rangle / U_\infty$  at different heights  $X$  above the bluff-body base. Experimental PIV data for test case 1 are shown as  $\bullet$ , simulations results are  $(-)$  for test case 1,  $(\star)$  for test case 2, and  $(\circ)$  for test case 3.

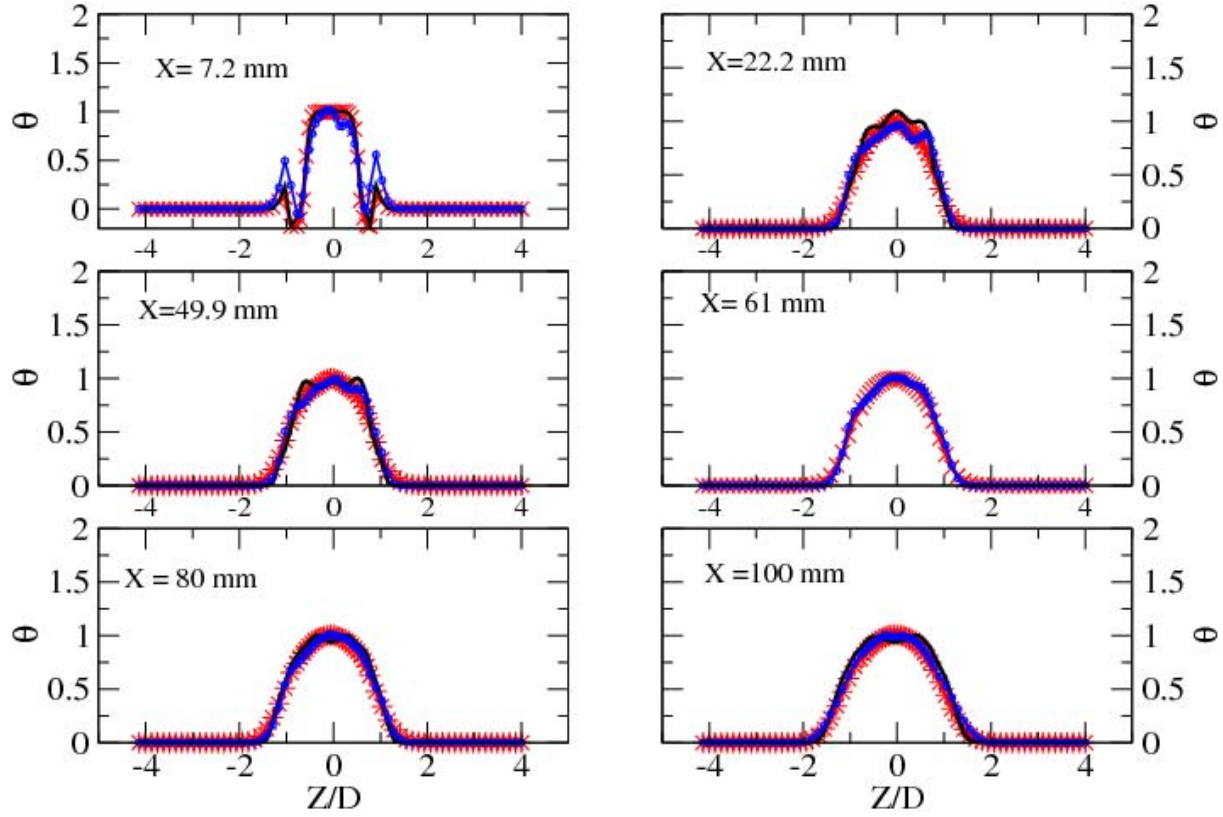


Figure 31: Time averaged non-dimensional temperature  $\Theta = (\langle \tilde{T} \rangle - T_\infty) / (T_{st} - T_\infty)$  at different heights above the bluff body base, (—) for test case 1, (★) for test case 2, and (○) for test case 3.  $T_{st}$  is the maximum burning temperature at stoichiometric conditions

( $Z = 0.021$ ). As the RZ tip oscillated, the strain rate changed across the flame surface, which was pushed outwards into the high-speed regions of the flow. Temperature variations showed up at the edge of the RZ, indicating high dissipation rates at these locations. Because of the shedding, alternative regions of hot and fresh gases were separated at the end of the RZ and convect downstream. These regions could grow in size as they progress downstream or they could remix with hot gases and burned out. The RZ provided sufficient residence time to mix and combust the fresh gases, which was shown in Fig. 32. Starting from Fig. 32a, a pocket of unburned gas appeared on the right just outside of the RZ. Figures 32c-32e show how a part of this unburned gas was entrained into the RZ, where it mixed with hot reaction products and burned. The remaining part of the pocket was convected downstream, where it gradually mixed and burned. While the RZ oscillated to the right because of the vortex shedding, another pocket of unburned gases was entrained into a region just left of the RZ, where it underwent a very similar process as the previous pocket on the right. This process repeated in every cycle on both sides.

The same analysis could be performed for test case 3, shown in Fig. 33. The flame showed wake and flame structure similar to the first flame. The RZ extended around 50 mm above the bluff-body base. The oscillation frequency was higher at 196 Hz, as the residence time was smaller in this case, but the Strouhal number was very comparable to the first case. The Strouhal numbers for all three cases were very close to 0.2. The values are given in Table 1. The table demonstrates that the overall dynamics of all three cases agreed quite well, which again confirmed the applicability of the Damköhler number similarity concept, as presented in this report.

### 3.1.5 Conclusion

The existence of Damköhler number similarity for static stability in augmentor flows was demonstrated. A high-speed/fast-chemistry flame was shown to have similar mean velocity and temperature fields, lift-off height, and dynamic behavior as the low-speed/slow chemistry flames. While the present study did not consider actual blow-off, these characteristics have been used as surrogates for static stability. A characteristic Damköhler number was defined based on the maximum chemical production rate of the progress variable. It was shown that, for all cases studied, the mean velocity and temperature fields, as well as the frequency of the bluff-body wake oscillation, showed self-similar behavior.

## 3.2 Large-Eddy Simulations of New Flame Holder Geometries

In Section 2, experimental studies were used to assess the performance of improved flame-holder designs for augmentors. Here, we performed numerical simulations of the same experimental setup to assess the ability of the models to predict the improved stability observed in the new designs. If successful, the use of simulation allowed for the analysis of the different flow



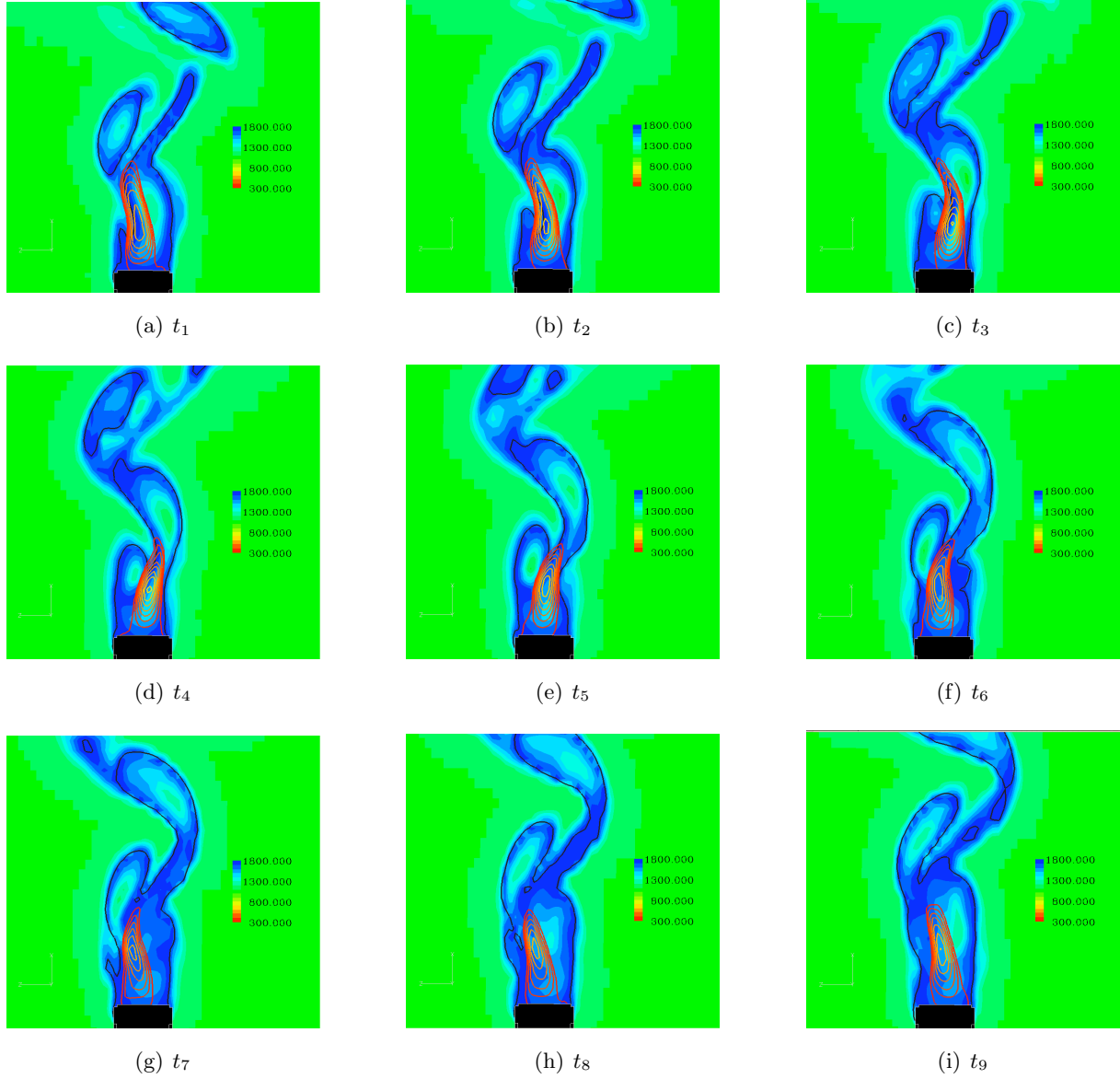


Figure 32: Instantaneous temperature distribution for case 1 combined with the contours of negative axial velocity (red lines) and the contour of stoichiometric mixture fraction (black line) over a complete shedding cycle

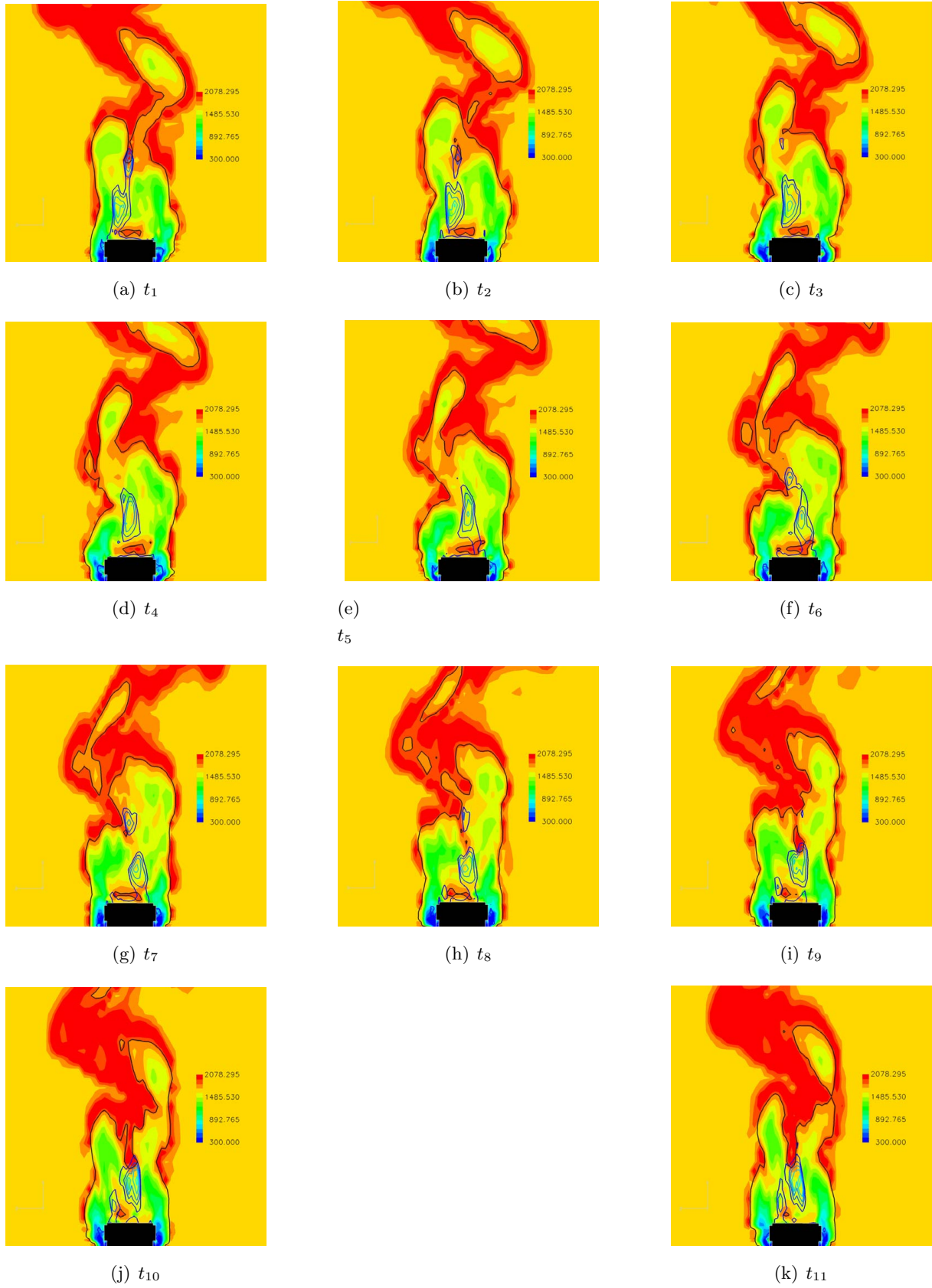


Figure 33: Instantaneous temperature distribution for case 3 combined with contours of negative axial velocity (red lines) and the contour of stoichiometric mixture fraction (black line) over a complete shedding cycle

structures induced by the different bluff body shapes and their impact on flame stability. The interaction of the different injection holes, for example, could be studied in detail and optimized using numerical simulations. As another example, the presence of localized regions of high fuel concentration that was expected in the local cavity shape designs could be investigated with simulations. Thus, simulation could be a valuable tool in the design and development of new bluff body shapes for improved flame stability.

### 3.2.1 Test Cases and Simulation Setup

In order to test the modeling capabilities, we computed a subset of the geometries introduced in Section 2. The entire three-dimensional experimental setup was modeled, along with the six different injection holes. A cartesian grid with local stretching was used to represent the setup. The generated computational grid is shown in Fig. 34. The grid size was  $192 \times 384 \times 192$  in the

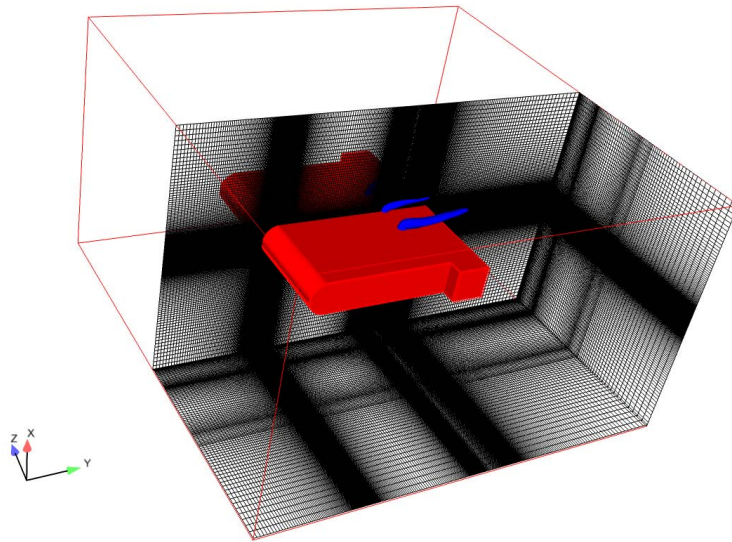


Figure 34: Grid used for the computational study. The reference shape was modeled in the case shown here. The blue region represents the methane fuel emanating from the injection holes.

directions  $x$ ,  $y$ , and  $z$ . As in the experiments,  $x$  was the direction aligned with the methane injection,  $y$  was the direction of the vitiated stream flow, and  $z$  was the third direction. The location of the different holes can be seen in Fig. 34. Appropriate stretching was introduced to resolve the geometric shapes adequately. The simulation of the entire channel was avoided by trimming the domain to 8 inches wide in the  $x$  direction and 14 inches in the  $z$  direction. A zero velocity gradient condition was applied on the lateral surfaces. The extent in the  $y$  direction was 4 inches upstream and 5 inches downstream of the bluff body. The crossflow had a bulk velocity of 5 m/s and a turbulence intensity of 8 %. An isotropic turbulence field was generated

and injected at the vitiated air inflow at the rate of the bulk velocity. The temperature of the crossflow was set to 1315 K based on experimental measurements. The composition of the crossflow was obtained through a premixed combustion calculation for an equivalence ratio of 0.67. The methane jet had an initial temperature of 400 K and the same momentum flux as the crossflow.

The experimental cases used for the study were the Reference case, the D+S (in-phase), and the T shapes. The geometries for the different cases are depicted in Fig. 4. It was found in the experiment that the Reference case had a high liftoff height of around 37 mm. The D+S shape had localized cavities, which caused a lower liftoff height of around 17 mm. The T shape also had a small liftoff height of around 22 mm. The cases were chosen to span the range from low liftoff to high liftoff. Modeling these geometrically varied shapes was also a good test of the robustness of the numerical simulation code.

### 3.2.2 Sub-Filter Models and Numerical Schemes

The code used for this study was a high-order kinetic energy conserving code. The description of the code and the equations solved has been provided previously in Section 3.1.2. LES studies were performed by solving the filtered flow equations that were presented earlier. A dynamic Smagorinsky model with Lagrangian averaging was used to model the sub-filter stresses. The chemistry in the simulation was solved using the Flamelet Progress Variable model (FPV) described in the previous section. The chemistry was parameterized as function of the progress variable ( $\tilde{C}$ ), mean mixture fraction ( $\tilde{Z}$ ) and the variance of the mixture fraction ( $\tilde{Z}''^2$ ). The composition at zero mixture fraction corresponded to the conditions of the vitiated crossflow. A unity mixture fraction value corresponded to pure methane fuel.

### 3.2.3 Results

The two-dimensional instantaneous velocity fields for the three different cases are shown in Fig. 35 for the Pxy\_C plane. The flow features in the simulation were similar to those observed in the experiments. A stagnation region formed upstream of the bluff body, as expected. The methane jets in the crossflow should lead to a stagnation region downstream of the jets, which was observed in the simulation results. Downstream of the bluff body, recirculation regions were formed for all three cases. The recirculation region was found to be closer for the T and D+S shapes than the Reference case. This trend also was seen in the experiments. Centerline profiles of vertical velocity downstream of the bluff body are shown in Fig. 36. The velocity profiles compared reasonably well with the experimental plot shown in Fig. 10d for the reference and the triangle cases. For the D+S case, the velocity was higher than the experiment, but a similar trend is observed.

The temperature distributions for the different cases are presented in Fig. 37. The stoichiometric mixture fraction iso-surface also is indicated in these plots by the black line. The mass

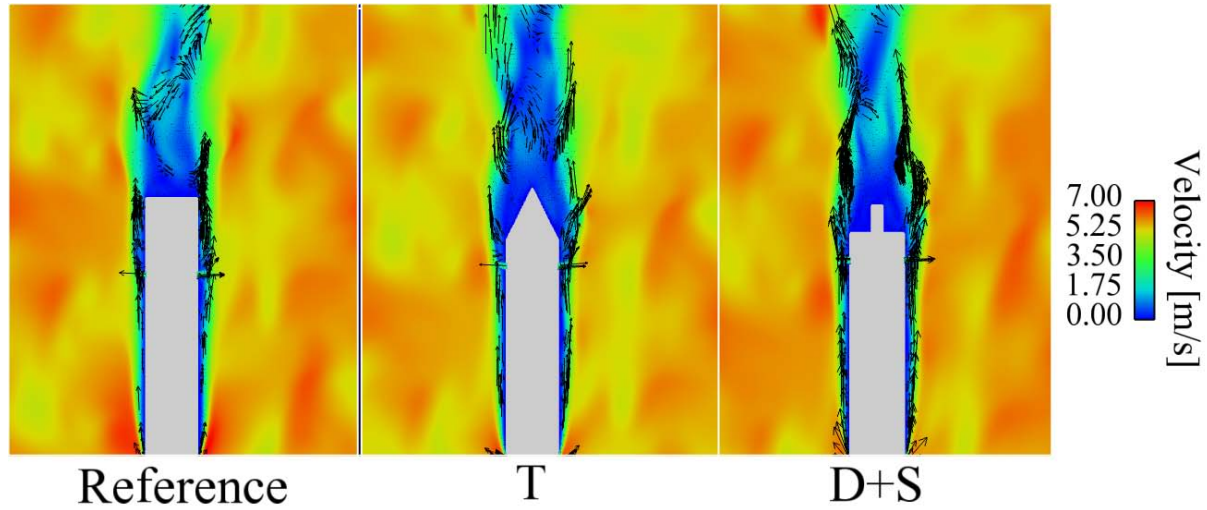


Figure 35: Instantaneous velocity magnitude field for the three different bluff body shapes.

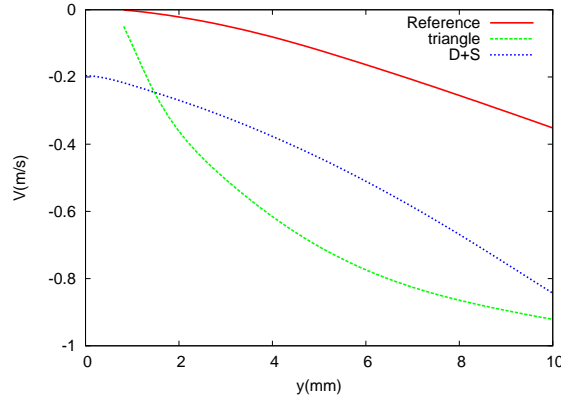


Figure 36: Computed vertical velocity profiles in the  $y$  direction along the centerline.

fraction of the CH radical is shown in Fig. 38 to compare with visual images of CH from the experiments. Flames were seen for all cases at some distance downstream of the jets; however, there were significant differences from the experimental results. The main difference was that the flames form on the edge of the bluff body wake, which was not seen in the experiment. Furthermore, the flame was attached to the flame holder in the region downstream of the bluff body for all computed cases, which also was not observed in the experiments. In the simulation, the mixture fraction was close to stoichiometric on the edges of the wake regions, which could be observed in Fig. 37. Thus, it was reasonable to see a high temperature region, since the flame typically had the highest temperature close to stoichiometric. Such an attached flame along with the wake edge flame was seen in the experiments for certain design geometries. Examples were shown in the phase I report. It was found in the experiments that introducing the tur-

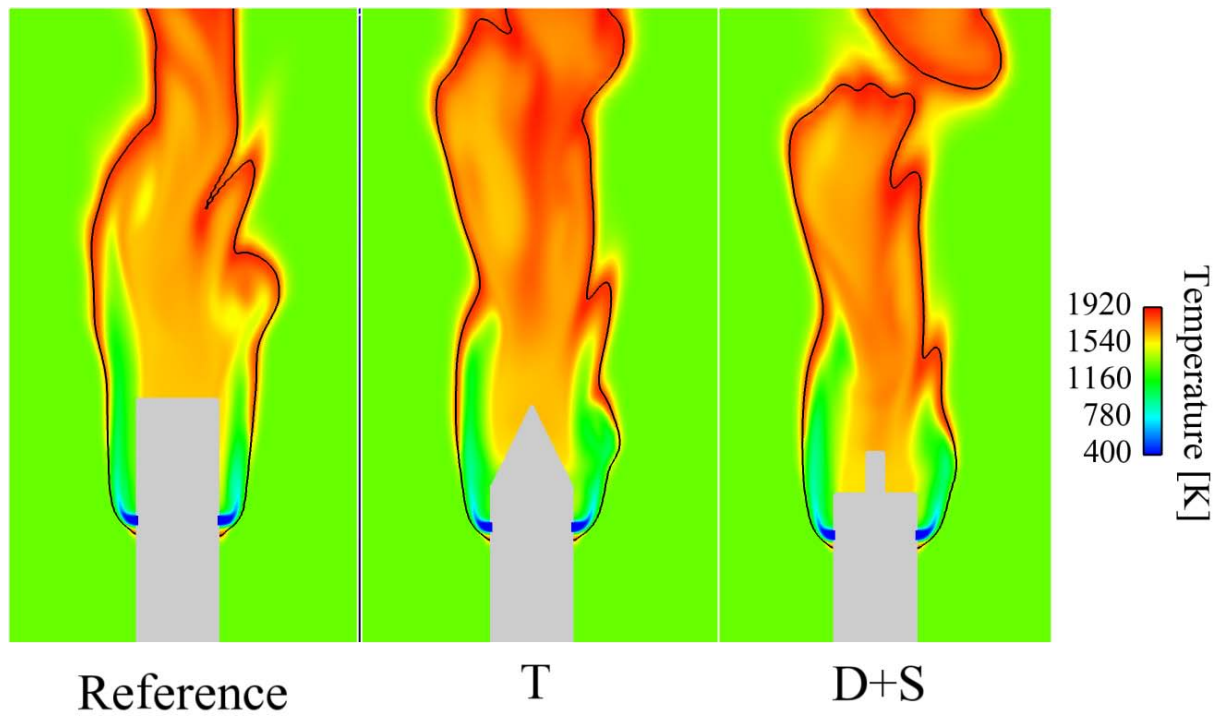


Figure 37: Instantaneous temperature fields for the three different bluff body shapes. The black line represents the iso-contour of stoichiometric mixture fraction.

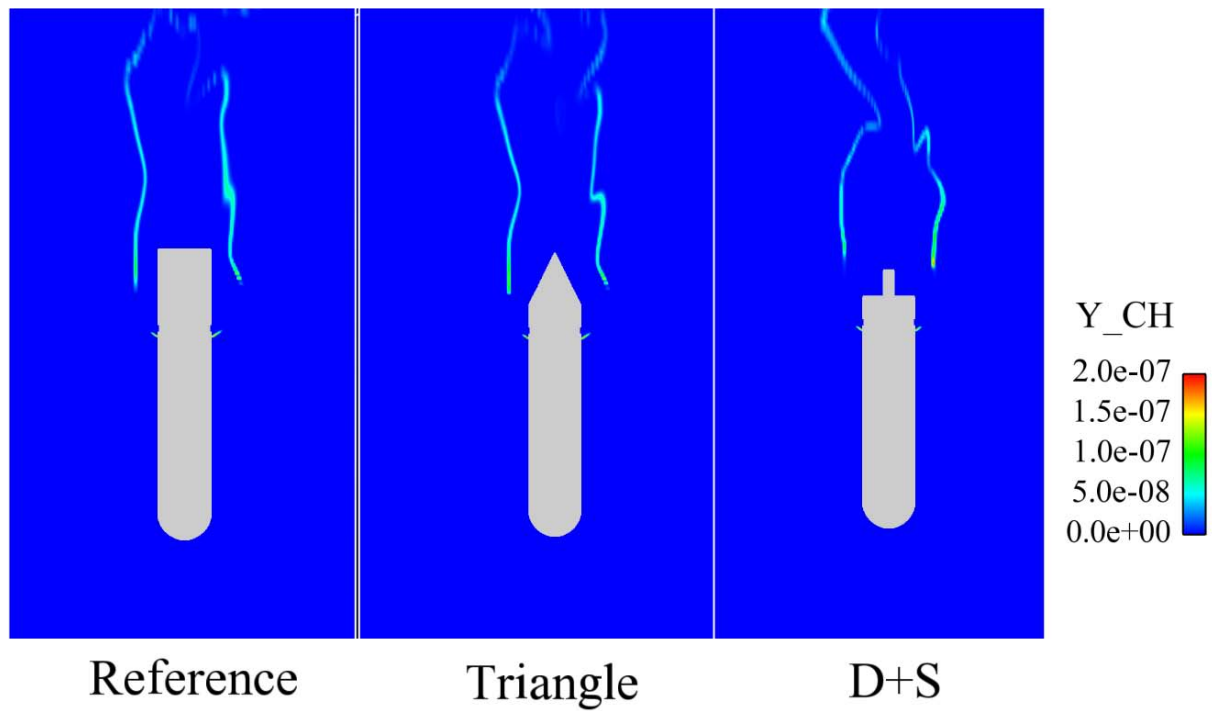


Figure 38: Instantaneous CH field for the three different bluff body shapes.

bulence mesh changed the flame topology from a jet-stabilized to a wake stabilized flame. The effect of the turbulence grid was represented by using isotropic turbulence at the inlet at the measured turbulence level; however, this turbulence grid model might not be accurate enough, and the turbulence mesh would be computed explicitly in the future. It also was possible that the liftoff was sensitive to other boundary conditions or modeling assumptions prescribed in the simulations. We therefore performed a sensitivity study to test the importance of some of the assumptions in the simulations.

Among the conditions specified, the vitiated flow temperature was particularly important for the flame characteristics. Its effect was studied here by varying the inlet temperature to 1200 K and 1100 K. Another assumption made in the chemical model used for the simulations was the use of unity Lewis numbers. The justification for selecting unity Lewis number was that in turbulent flows, the turbulence was usually intense enough that turbulent diffusivity dominates molecular diffusivity. Thus, all species diffused in a similar way. The effect of this assumption was tested by performing an additional simulation using non-unity Lewis numbers.

#### **3.2.4 Effect of Crossflow Temperature**

The crossflow temperature was varied to 1100 K and 1200 K to see the sensitivity of the flame location to this parameter. The experimentally measured crossflow temperature was 1315 K. This variation was done for the reference shape of the bluff body. It was found for both these cases that the wake edge flames were still present. The flame also was attached to the bluff body for these cases. Uncertainties in the crossflow temperature therefore could not explain the observed differences with the experiment.

#### **3.2.5 Effect of Lewis number Approximation**

The influence of non-uniform diffusion was checked by performing an additional simulation with non-unity Lewis numbers. For this simulation, the crossflow temperature was set to the experimentally measured value of 1315 K. The simulation was performed for the reference shape of the bluff body. The results for the CH mass fraction and temperature are shown in Fig. 39. The Lewis number did not have a significant effect on the results. Both the temperature and CH mass fraction were similar to the results assuming unity Lewis numbers.

#### **3.2.6 Conclusions**

The experimental setup used to study bluff body shapes in augmentors was simulated using large eddy simulation. The velocity comparisons illustrated that the simulation had similar flow features as were observed in the experiments. The temperature and the CH mass fractions showed that the flame was attached to the bluff body for all cases. Also, flames formed on the edge of the bluff body wake. Both these features were not seen in the experiments. The effect of boundary condition uncertainty and the unity Lewis number assumption in the model were



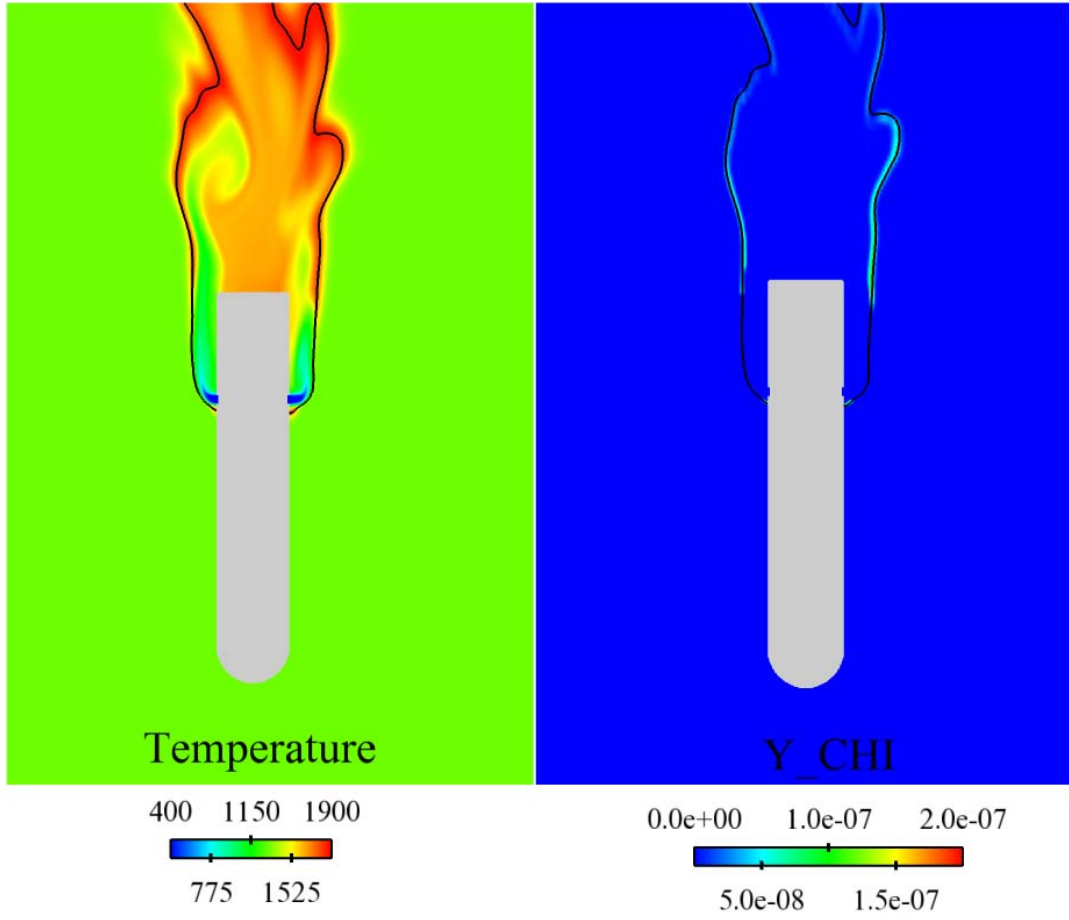


Figure 39: Instantaneous temperature and CH field for the non-unity Lewis number study. The black line represents the isocontour of stoichiometric mixture fraction.

investigated by performing additional simulations with varied crossflow temperature and with the non-unity Lewis number assumption. Both sensitivity studies did not reveal a significant effect.

It was speculated that the reason for disagreement was a higher level of inflow turbulence in the experiment or a very non-isotropic flow induced by the turbulence mesh. The cited reason was confirmed by several observations: i) flame stabilization on the fuel jets was observed in the phase I experiments. After adding the turbulence grid, the stabilization point in the experiments moved into the wake of the bluff body, which confirmed the importance of the incoming turbulence. ii) The CH chemiluminescence plots in Fig. 3 showed substantial turbulence in the wake region, which was not observed in the simulations and which probably originated from the inflow turbulence. iii) The inflow velocity profile and Reynolds stress tensor were not very well quantified in the experiment; therefore the prescribed values had high uncertainty.

In the future, we shall use the AFRL experiments of the flame holders proposed here for further validation.



## Appendix A

### A.1 Contributors

Prof. Heinz Pitsch	Stanford University
Prof. Godfrey Mungal	Stanford University
Dr. Frank Ham	Stanford University
Dr. Shoreh Hajiloo	Cascade Technologies
Dr. Wookyung Kim	Stanford University
Dr. Mohammad Shoeybi	Cascade Technologies
Dr. Hung Le	Cascade Technologies
Dr. Hyungrok Do	Stanford University
Mr. Seong-kyun Im	Stanford University

### A.2 Related Publications & Presentations

1. Hossam El-Asrag, Heinz Pitsch, Wookyung Kim, Hyungrok Do & M. Godfrey Mungal, Flame Stability in Augmentor Flows, *Comb. Sci. Tech.*, submitted, 2010.
2. Hossam El-Asrag, Heinz Pitsch, Wookyung Kim, Hyungrok Do & M. Godfrey Mungal, A Computational and Experimental Assessment of the Damköhler Number Similarity for Static Flame Stability in Augmentor Flows, *AIAA-paper AIAA*, 2008–4955, 2008.
3. Wookyung Kim, Seong-kyun Im, Hyungrok Do & M. G. Mungal, Stereo PIV Measurements of a Geometrically Modified Flame Augmentor Base, *PIV09, 8th International Symposium on Particle Image Velocimetry*, August 25-28, 2009, Melbourne, Australia.
4. Wookyung Kim, Seong-kyun Im, Hyungrok Do & M. G. Mungal, Flame Liftoff Height Dependence on Geometrically Modified Bluff Bodies in a Vitiated Flow, *Expts. Fluids*, 49, 27–41, 2010.
5. Wookyung Kim, Hyungrok Do & M. G. Mungal, The improvement of blowout limit in partially/fully premixed flames with geometrically modified bluffbody bases, *Expts. Fluids*, submitted.
6. Wookyung Kim, Seong-kyun Im, Hyungrok Do & M. G. Mungal, The Role of Local Base Cavities in an Augmentor Bluffbody Flameholder, *to be presented at the AIAA-ASM 49th Aerospace Sciences Meeting*, January 4-7, 2011, Orlando, FL.
7. Frank Ham, Heinz Pitsch, Godfrey Mungal, A Computational and Experimental Assessment of the Damköhler Number Similarity for Static Flame Stability in Augmentor Flows, *presented at the Augmentor System Design Conference*, March 18, 2010, Jacksonville, FL.

## References

- CHRISTENSEN, K. T. & WU, Y. 2005 Visualization and characterization of small-scale spanwise vortices in turbulent channel flow. *J. Visualization* **8**, 177–185.
- DESJARDINS, O., BLANQUART, G., BALARAC, G. & PITSCH, H. 2008 High order conservative finite difference scheme for variable density low mach number turbulent flows. *Journal of Computational Physics* **227** (15), 7125–7159.
- GHONIEM, A. F. & KRISHNAN, A. 1988 Origin and manifestation of flow-combustion interactions in premixed shear layer. *Proc. Combust. Inst.* **22**, 665–675.
- IHME, M., CHA, C. M. & PITSCH, H. 2005 Prediction of local extinction and re-ignition effects in non-premixed turbulent combustion using a flamelet/progress variable approach. *Proceedings of the Combustion Institute* **30**, 793–800.
- IHME, M. & PITSCH, H. 2008a Modeling of radiation and soot formation in turbulent non-premixed flames using a flamelet/progress variable formulation. *Phys. Fluids* **20** (5), Art. No. 055110.
- IHME, M. & PITSCH, H. 2008b Prediction of extinction and reignition in non-premixed turbulent flames using a flamelet/progress variable model. part 1: A priori study and presumed pdf closure. *Comb. Flame* **155** (1-2), 70–89.
- IHME, M. & PITSCH, H. 2008c Prediction of extinction and reignition in non-premixed turbulent flames using a flamelet/progress variable model. part 2: Application in les of sandia flames d and e. *Comb. Flame* **155** (1-2), 90–107.
- KANG, S., IACCARINO, G., HAM, F. & MOIN, P. 2009 Prediction of wall-pressure fluctuation in turbulent flows with an immersed boundary method. *J. Comput. Phys.* **229** (9), 3189–3208.
- KHOSLA, S., LEACH, T. T. & SMITH, C. E. 2007 Flame stabilization and role of von karman vortex shedding behind bluff body flameholders. In *43rd AIAA/ASME/SAE/ASEE Joint Propulsion Conf. and Exhibit, Cincinnati, OH, USA*.
- KIEL, B., GARWICK, K., GORD, J. R., MILLER, J., LYNCH, A., HILL, R. & PHILLIPS, S. 2007 A detailed investigation of bluff-body stabilized flames. In *45<sup>th</sup> AIAA Aerospace Sciences Meeting and Exhibit, Reno, Nevada, AIAA 2007-168*.
- KIEL, B., GARWICK, K., LYNCH, A., GORD, J. R. & MEYER, T. 2006 Non-reacting and combustor flow investigation of bluff-bodies in cross flow. In *42<sup>nd</sup> AIAA/ASME/SAE/ASEE Joint Propulsion Conference 9-12 July, 2006, Sacramento, AIAA 2006-5234*.
- KING, C. R. & NAKANISHI, S. 1957 Effects of some configuration changes on afterburner combustion performance. *NACA Report, NACA-RM-E57C01*.

- KNAUS, D. A., MAGARI, P. J., HILL, R. W., PHILLIPS, S. D. & KIEL, B. V. 2008 Predicting augmentor static stability using local damköhler number. In *46<sup>th</sup> AIAA Sciences Meeting and Exhibit, 7 - 10 January 2008, Reno, NV, AIAA 2008-1027*.
- KURIMOTO, N., SUZUKI, Y. & KASAGI, N. 2004 Coaxial jet control for lifted flame stabilization with arrayed miniature actuators. In *12th International Symposium on Applications of Laser Techniques, Lisbon, Portugal*.
- LIEUWEN, T., SHANBOUGE, S., KHOSLA, S. & SMITH, C. 2007 Dynamics of bluff-body flames near blow-off. In *45<sup>th</sup> AIAA Aerospace Sciences Meeting and Exhibit, Reno, Nevada, AIAA 2006 0152*.
- LONGWELL, J. P., FOREST, E. E. & WEISS, M. A. 1953 Flame stability in bluff-body recirculation zones. *Journal of Industrial and Engineering Chemistry* **45**, 1629–1633.
- MEHTA, P. G. & SOTERIOU, M. C. 2003 Combustion heat release effects on the dynamics of bluff-body stabilized premixed reacting flows. In *41<sup>th</sup> AIAA Aerospace Sciences Meeting and Exhibit, Reno, Nevada, AIAA 2003-835*.
- MELLOR, A. M. 1980 Semi-empirical correlations for gas turbine emissions, ignition, and flame stabilization. *Prog. Energ. Comb. Sci.* **6** (4), 347–358.
- MOIN, P., SQUIRES, K., CABOT, W. & LEE, S. 1991 A dynamic subgrid-scale model for compressible turbulence and scalar transport. *Physics of Fluid A* **3**, 2746–2757.
- MORINISHI, Y., LUND, O. V., VASILYEV, O. V. & MOIN, P. 1998 Fully conservative higher order finite difference schemes for compressible flow. *Journal of Computational Physics* **143**, 90 – 124.
- NATRAJAN, V. K. & CHRISTENSEN, K. T. 2006 The role of coherent structures in subgrid-scale energy transfer within the log layer of wall turbulence. *Phys. Fluids* **18**, 065104.
- PASCHEREIT, C. O., FLOHR, P. & GUTMARK, E. J. 2006 Combustion control by vortex breakdown stabilization. *J. Turbo Mach.* **128**, 679–688.
- PETERS, N. 1984 Laminar diffusion flamelet models in non-premixed turbulent combustion. *Progress of Energy and Combustion Science* **10**, 319–339.
- PIERCE, C. D. & MOIN, P. 1998 A dynamic model for subgrid-scale variance and dissipation rate of a conserved scalar simulation of non-premixed turbulent combustion. *Physics of Fluid* **10**, 3041–3044.
- PIERCE, C. D. & MOIN, P. 2001 *Progress-Variable Approach for Large-Eddy Simulation of Turbulent Combustion*. Mechanical Engineering Department Report, TF-80, Stanford University.

- PIERCE, C. D. & MOIN, P. 2004 Progress-variable approach for large-eddy simulation of non-premixed turbulent combustion. *Journal of Fluid Mechanics* **504**, 73–97.
- PITSCH, H. 2006 Large eddy simulation of turbulent combustion. *Annual Review of Fluid Mechanics* **38**, 453 – 482.
- PITSCH, H., CHA, C. M. & FEDOTOV, S. 2003 Flamelet modeling of non-premixed turbulent combustion with local extinction and re-ignition. *Combustion Theory and Modeling* **7**, 317–332.
- PITSCH, H. & FEDOTOV, S. 2001 Investigation of scalar dissipation rate fluctuations in non-premixed turbulent combustion using a stochastic approach. *Combustion Theory and Modeling* **5**, 41–57.
- PORUMBEL, I. & MENON, S. 2006 Large eddy simulation of bluff body stabilized premixed flame. In *44<sup>th</sup> AIAA Aerospace Sciences Meeting and Exhibit, Reno, Nevada, AIAA 2006 0152*.
- RADHAKRISHNAN, K., HEYWOOD, J. B. & TABACZYNSKI, R. J. 1981 Premixed turbulent flame blowoff velocity correlation based on coherent structures in turbulent flows. *Comb. Flame* **42** (1), 19–33.
- ROACH, J. M., FISHER, T. C., FRANKEL, S. H., SEKAR, B. & KIEL, B. V. 2008 Cfd predictions of damköhler number fields for reduced order modeling of v-gutter flame stability. In *46<sup>th</sup> AIAA Sciences Meeting and Exhibit, 7 - 10 January 2008, Reno, NV, AIAA 2008-0509*.
- SHANBHOGUE, J. J., HUSAIN, S. & LIEUWEN, T. 2009a Lean blowoff of bluff body stabilized flames: Scaling and dynamics. *Prog. Energ. Comb. Sci.* **35**, 98–120.
- SHANBHOGUE, S. J., HUSAIN, S. & LIEUWEN, T. 2009b Lean blowoff of bluff body stabilized flames: Scaling and dynamics. *Prog. in Energy and Combust. Sci.* **35**, 98–120.
- SHIN, D. S. & FERZIGER, J. H. 1991 Linear stability of the reacting mixing layer. *AIAA Journal* **29**, 1634–1642.
- SMITH, S. H. & MUNGAL, M. G. 1998 Mixing, structure and scaling of the jet in crossflow. *J. Fluid Mech.* **357**, 83–122.
- SOVRAN, G., MOREL, T. & MASON, W. T. 1978 *Aerodynamic drag mechanisms of bluff bodies and road vehicles*. Plenum Press, New York.
- STWALLEY, R. M. & LEFEBVRE, A. H. 1988 Flame stabilization using large flameholders of irregular shape. *J. Propulsion* **4**, 4–13.

- SURAJ, N. & LIEUWEN, T. 2007 Near-blowoff dynamics of a bluff-body stabilized flame. *Journal of Propulsion and Power* **23** (2), 421 – 427.
- ZUKOWSKI, E. E. & MARBLE, F. E. 1955 The role of wake transition in the process of flame stabilization on bluff-bodies. In *AGARD Combustion Researches and Reviews*, pp. 167–180. Butterworth Scientific Publishers, London.